

Short-term synaptic plasticity optimally models continuous environments

Timoleon Moraitis*, Abu Sebastian, and Evangelos Eleftheriou
 IBM Research – Zurich, 8803 Rüschlikon, Switzerland
 Email: *timosmoraitis@gmail.com

Biological neural networks operate with extraordinary energy efficiency, owing to properties¹⁻³ such as spike-based communication and synaptic plasticity driven by local activity.⁴⁻⁶ When emulated *in silico*, such properties also enable highly energy-efficient machine learning and inference systems.⁷⁻¹¹ However, it is unclear whether these mechanisms only trade off performance for efficiency or rather they are partly responsible for the superiority of biological intelligence. Here, we first address this theoretically, proving rigorously that indeed the optimal prediction and inference of randomly but continuously transforming environments, a common natural setting, relies on adaptivity through short-term spike-timing dependent plasticity, a hallmark of biological neural networks. Secondly, we assess this theoretical optimality via simulations and also demonstrate improved artificial intelligence (AI). For the first time, a largely biologically modelled spiking neural network (SNN) surpasses state-of-the-art artificial neural networks (ANNs) in all relevant aspects, in an example task of recognizing video frames transformed by moving occlusions. The SNN recognizes the frames more accurately, even if trained on few, still, and untransformed images, with unsupervised and synaptically-local learning, binary spikes, and a single layer of neurons – all in contrast to the deep-learning-trained ANNs. These results indicate that on-line adaptivity and spike-based computation may optimize natural intelligence for natural environments. Moreover, this expands the goal of exploiting biological neuro-synaptic properties for AI, from mere efficiency, to computational supremacy altogether.

Fundamental operational principles of biological neural networks like those in the central nervous system (CNS)¹⁻³ are not part of the functionality of even the most successful ANN algorithms. A key aspect of spiking neurons is their communication by use of action potentials, i.e. stereotypical voltage spikes, which carry information in their timing. In addition, to process and learn from this timing information, synapses, i.e. connections between neurons, are equipped with plasticity mechanisms, which dynamically change the synaptic efficacy, i.e. strength, depending on the timing of postsynaptic and/or presynaptic spikes. For example, spike-timing-dependent plasticity (STDP) is a Hebbian, i.e. associative, plasticity, where pairs of pre- and post-synaptic spikes induce changes to the synaptic strength dependent on the order and latency of the spike pair.¹²⁻¹⁴ Plastic changes can be long-term or short-term. Short-term plasticity (STP)¹⁵⁻¹⁷ has been shown for instance to act as a signal-filtering mechanism,¹⁸ and to focus learning on selective timescales of the input by interacting with STDP.^{19,20} Such spike-based biophysical mechanisms have been emulated by the physics of electronics to implement neuromorphic computing systems. Silicon spiking neurons, synapses, and

neuromorphic processors are extremely power-efficient⁷⁻¹¹ and have shown particular promise in tasks such as interfacing with biological neurons, including chips learning to interpret brain activity.^{21,22} But the human brain exceeds current ANNs by far not only in terms of efficiency, but also in its end performance in demanding tasks. Identifying the source of this computational advantage is an important goal for the neurosciences and could also lead to better AI. It is reasonable to speculate that spike-based computational mechanisms may also be part of the reason for this performance advantage. Indeed, there is evidence that the brain's powerful computations emerge from simple neural circuits with spike-based plasticity. For example, the brain is well-documented to maintain statistically optimal internal models of the environment.²³⁻³¹ Spiking neurons can give rise to such Bayesian models, whereas STDP can form and update them to account for new observations.³² The structure of such SNNs is considered canonical in the brain's neocortex.³³ Their function through STDP is akin to on-line clustering or expectation-maximization,³² and their models can be applied to common benchmarking tasks of machine learning.³⁴ Proposals for functionality unique to SNNs have also been presented,^{1,20} including models³⁵ with very recent experimental confirmation³⁶ that individual spiking neurons in the primate brain, even a single compartment thereof, can compute functions that were traditionally considered to require multiple layers of conventional artificial neural networks (ANNs). Nevertheless, in concrete terms, thus far the accuracy that is achievable by brain-inspired SNNs in tasks of machine intelligence has trailed that of ANNs,³⁷⁻⁴⁰ and there is little theoretical understanding of SNN-native properties in a machine-learning context.^{32,41} As a result, not only do the benefits in AI accuracy from SNN mechanisms remain hypothetical, but it is also unclear if these mechanisms are responsible for any of the brain's superiority to AI. In this article, we show that, in a common problem setting – namely, prediction and inference of environments with random but continuous dynamics – not only do biological computational mechanisms of SNNs implement a solution, they are indeed the theoretically optimal model, and can outperform ANNs.

ST-STDP reflects the dynamics of natural environments

We model the environment as a set of objects, each belonging to one of K classes. Each object can transform in a random or unknown, but time-continuous manner. To predict future transformations and infer their class, an observer observes the environment. Only one object is observed at each time instance, and the observer switches to different objects at random instances (Fig. 1 a). In the absence of additional prior knowledge about an object's dynamics, a future observation of the potentially transformed object is distributed around its most recent observation (Fig. 1 b; also see Methods section). In addition, time and space continuity imply

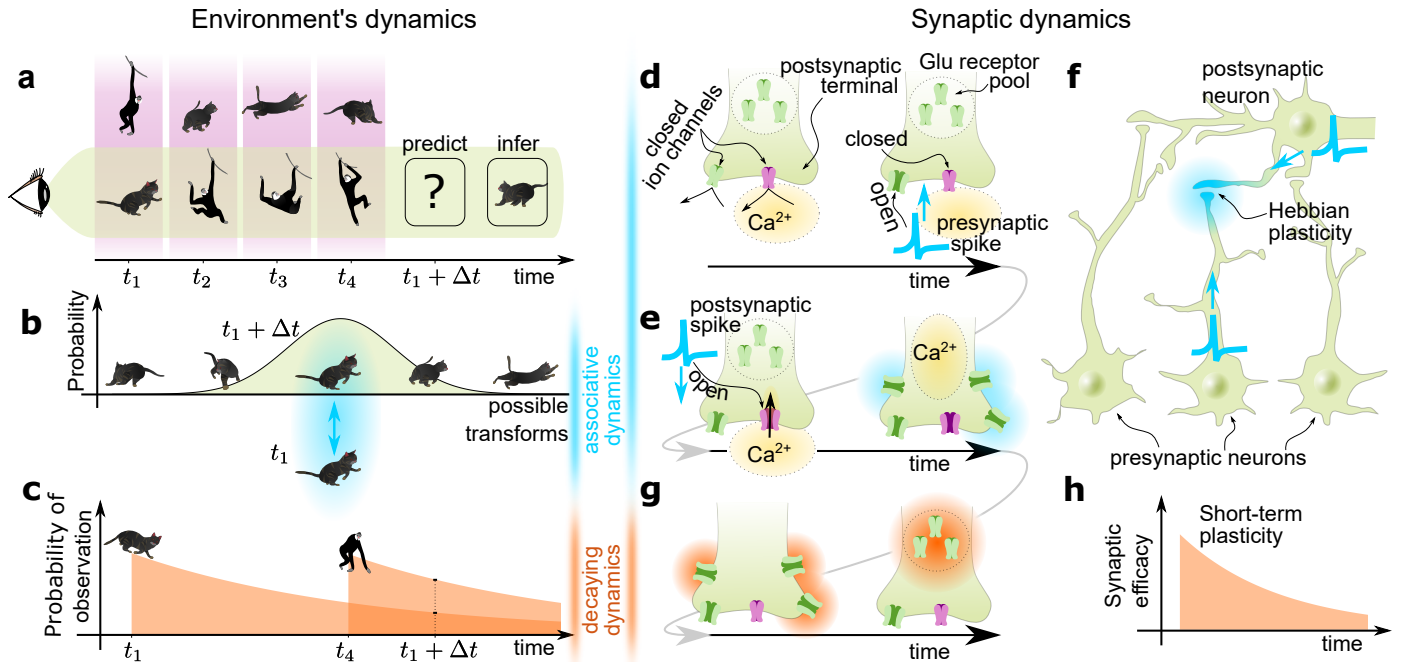


Figure 1: Analogous dynamics between natural environments and synapses. **a**, An environment (here, a visual one, depicted by the magenta field) contains objects (e.g. cat and gibbon) that transform and move randomly but continuously. An observer (left, eye) observes (green field) one object at a time. Objects are replaced at random time instances (e.g. t_2). The observer aims to maintain a model of the environment that can predict future observations (question mark) and infer their type (frame labelled “infer”). **b**, An object’s observation (t_1 , bottom cat) implies that the probability distribution of future ($t_1 + \Delta t$) transforms of this object (horizontal axis) is centred around its last observation. **c**, An observed object (t_1 , cat, and t_4 , gibbon) is likely to be observed again soon after, but less so as time passes (decaying curves). **d**, Left: A synapse’s postsynaptic terminal has ion channels that are resting closed, preventing ions, e.g. Ca^{2+} , from entering the postsynaptic neuron. Right: A presynaptic spike releases neurotransmitters, e.g. glutamate (Glu) that attach to ion channel receptors and open some channels, but do not suffice to open Ca^{2+} channels, which are postsynaptic-voltage-gated. The synapse includes a pool of additional inactive Glu receptors. **e**, In the event of an immediately subsequent postsynaptic spike, channels open, allowing Ca^{2+} to enter (left), which has a potentiating effect on the activity and the number of Glu receptors on the membrane (right, blue highlight). This increases the efficacy of the synapse, and is observed as STDP. **f**, This establishes a Hebbian link associating only the causally activated pre- and post-synaptic neurons. **g**, As Ca^{2+} ’s effect on the Glu receptor pool decays with time (orange highlight), then, **h**, the efficacy of the synapse also decays towards its original resting weight, and is observed as STP, so the overall effect amounts to ST-STDP. Synaptic dynamics are analogous to the environment’s dynamics (associative dynamics: blue elements, compare d-f vs b; decaying dynamics: orange elements, compare g-h vs c). We show analytically that computations performed by such synapses provide the optimal solution to task (a) of the observer.

that an observed object is likely to be observed again immediately after, but as objects move in space relative to the observer, this likelihood decays to zero with time, according to a function $f(t)$ (Fig. 1c and Supplementary Information, section S1). The model is rather general, as its main assumption is merely that the environment is continuous with random or unknown dynamics. Furthermore, there is no assumption of a specific sensory domain, i.e. transforming objects may range from visual patterns in a scene-understanding task, to proprioceptive representations of bodily states in motor control, to formations of technical indicators in financial forecasting, etc.

It can be seen that these common dynamics of natural environments bear significant analogies to the dynamics involved in ST-STDP. ST-STDP is a realization of STDP with short-term effects,⁴⁻⁶ and has been proposed as a mechanism for working memory in biological neural networks.^{42,43} It is observed in the early phase of long-term potentiation. A series of paired pre- followed by post-synaptic spikes can lead to a persistent increase in synaptic efficacy.⁴⁴⁻⁴⁶ However, when fewer stimuli are given, the induced change is short-term. This short-term increase in synaptic efficacy is mediated by a series of biophysical events (see Fig. 1d-h). A presynaptic action potential releases excitatory neurotransmitters such as glutamate (Glu), which attaches to receptors

of ion channels on the postsynaptic terminal, thus opening some of the channels (Fig. 1d). However, calcium channels with N-methyl-D-aspartate (NMDA) receptors are voltage-gated,⁴⁷ i.e. they only open if the postsynaptic voltage increases while Glu is attached. A postsynaptic spike occurring shortly after the presynaptic one achieves this, so that calcium does enter the postsynaptic cell. Calcium interacts with protein kinases that increase the activity and the number of Glu receptors on the postsynaptic membrane (Fig. 1e). This is observed as a Hebbian potentiation (Fig. 1f). The effect is short-term, as Glu receptors return to their resting state with a decay timescale as short as 1.6 minutes.⁶ Note that the associative memories formed through the Hebbian aspect of ST-STDP resemble the associative dynamics in the environment, i.e. the association of the last observation of an object with its most likely future form (Fig. 1, blue elements). In a second analogy, the transience of this potentiation could be used in computations to reflect the transiently decreasing probability of observing the same object again (Fig. 1, orange elements). Indeed, we performed a formal analysis that concluded that the Bayesian generative model of the future observations given the past ones requires for its optimality a mechanism equivalent to ST-STDP.

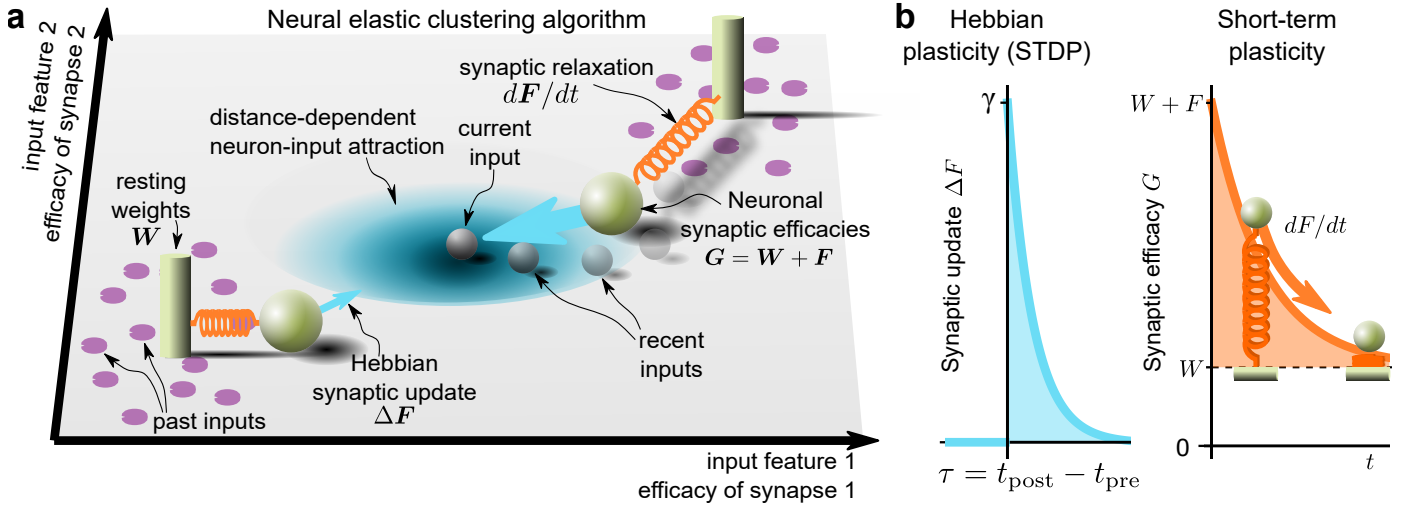


Figure 2: **Neural elastic clustering and underlying synaptic plasticity.** **a**, Random continuous environments are optimally modelled by a neurally-realizable clustering algorithm. Each cluster centroid (green spheres) corresponds to a neuron, here with two synapses, and is positioned in space according to its vector of synaptic efficacies \mathbf{G} . Recent inputs (transparent grey spheres) have pulled each neuron-centroid away from its fixed resting weight array \mathbf{W} (vertical poles), by a short-term component \mathbf{F} (orange spring). The neuron is constantly pulled back towards its resting state by a certain relaxation dynamics ($d\mathbf{F}/dt$, spring). A new input (grey sphere, centre) pulls each neuron by a $\Delta\mathbf{F}$ (blue arrow) that depends on the proximity between the input and the neuron (blue field), reflected by the neuron’s activation. **b**, The clustering algorithm is implemented by ST-STDP at the neurons’ synapses. The proximity-dependent updates of a neuron-centroid are determined by Hebbian plasticity. In case of spike-based rate-coded inputs, updates depend (blue curve) on the time difference τ between pre- and post-synaptic spikes. The relaxation of the neuron to its resting position with time is realized by short-term plasticity (orange curve). G , W , and F denote a representative synapse’s efficacy, resting weight, and dynamic term.

The neural elastic clustering algorithm

The derived generative model is equivalent to a neural circuit with ST-STDP (Supplementary Information, section S6.2), and is geometrically interpretable as a novel and intuitive clustering algorithm based on centroids with elastic positions (Fig. 2a, and Supplementary Information, section S5). Specifically, if input samples \mathbf{X}_t have n features, then each of the K classes is assigned a centroid, represented by a neuron with n input synapses. Thus, at each time instance t , the k -th neuron-centroid is lying in the n -dimensional space at a position determined by its vector of synaptic efficacies $\mathbf{G}_t^{(k)}$. A function of the sample’s proximity $u_t^{(k)}(\mathbf{X}_t)$ to this neuron determines the estimated likelihood $q^{(k)}(\mathbf{X}_t)$ of this sample conditional on it belonging to the k -th class $C^{(k)}$. Assuming that neurons enforce normalization of their synaptic efficacy arrays and receive normalized inputs, then the neuron defines its proximity to the input as the total weighted input, i.e. the cosine similarity $u_t^{(k)} = \frac{\mathbf{G}_t^{(k)} \cdot \mathbf{X}_t}{\|\mathbf{G}_t^{(k)}\| \cdot \|\mathbf{X}_t\|}$. An additional scalar parameter $G_t^{(0k)}$, represented in the neuron’s bias, accounts for the prior belief about this class’s probability. The bias parameterizes the neuron’s activation, which associates the sample with the k -th class $C^{(k)}$ as their joint probability. Ultimately, the activation of the k -th neuron-centroid relative to the other neurons, e.g. the argmax function as in K-means clustering, or the soft-max function, is the inference of the posterior probability $Q_t^{(k)}$ that the input belongs to $C^{(k)}$. Similarly to,³² we show that if the chosen relationship is soft-max and the neurons are linear, then the network’s output $Q_t^{(k)}$ is precisely the Bayesian inference given the present input and parameters (Supplementary Information, sections S3.1 and S6.2). The Bayesian generative model is the mixture, i.e. the weighted sum, of the K neurons’ likelihood functions $q^{(k)}(\mathbf{X}_t)$, which in this case are exponential, and is fully parameterized by the synaptic efficacies and neuronal biases.

The optimization rule of this model’s parameters, for the spa-

tiotemporal environments discussed in this article, is the elastic clustering algorithm. Specifically, we show (Supplementary Information, section S3.2) that, given the past observations, the model’s optimal Bayesian values for the synaptic efficacies comprise a fixed vector of resting weights $\mathbf{W}^{(k)}$ and a dynamic term $\mathbf{F}_t^{(k)}$ with a short-term memory, such that

$$\mathbf{G}_t^{(k)} = \mathbf{F}_t^{(k)} + \mathbf{W}^{(k)}. \quad (1)$$

The neuron-centroid initially lies at the resting position $\mathbf{W}^{(k)}$, which is found through conventional techniques such as expectation maximization. The synaptic efficacies remain optimal if at every posterior inference result $Q_t^{(k)}$ their dynamic term $\mathbf{F}_t^{(k)}$ is incremented by

$$\Delta\mathbf{F}_t^{(k)} = \gamma \mathbf{X}_t Q_t^{(k)}, \quad (2)$$

where γ is a positive constant, and if in addition, $\mathbf{F}_t^{(k)}$ subsequently decays continuously according to the dynamics $f(t)$ of the environment (Fig. 1c), such that $\mathbf{G}_t^{(k)}$ relaxes towards the fixed resting point $\mathbf{W}^{(k)}$. If $f(t)$ is exponential with a rate λ , then

$$\frac{d\mathbf{F}_t^{(k)}}{dt} = -\lambda \mathbf{F}_t^{(k)}. \quad (3)$$

The latter two equations describe the attraction of the centroid by the input, as well as its elasticity (Fig. 2a). The optimal bias $G_t^{(0k)}$ is also derived as consisting of a fixed term and a dynamic term. This dynamic term too is incremented at every inference step and relaxes with $f(t)$.

The derived solution (Eq. 1-3) dictates an ST-STDP rule for the synaptic efficacies (see Supplementary Information, section S6.2). In this direct equivalence, the attraction of the efficacy vector by the input proportionally to the output $Q_t^{(k)}$ (Eq. 2) is the Hebbian aspect of the plasticity. We also show that if input variables are

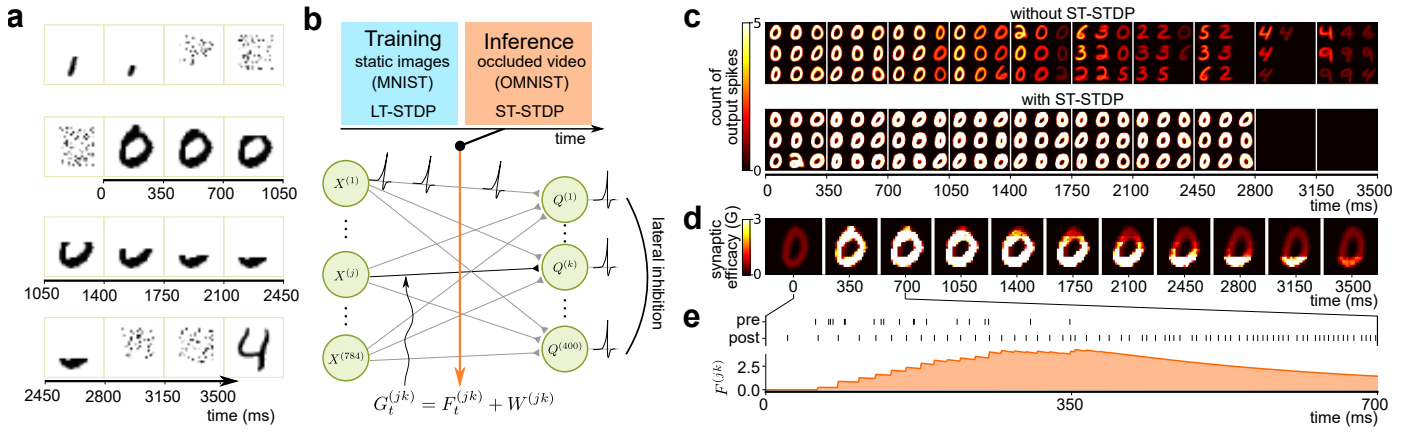


Figure 3: SNN with ST-STDP during stimulation by transforming visual inputs. **a**, A representative sequence of frames from the OMNIST set. The subsequence labelled as 0-3500 ms is the input used in the rest of the figure panels. **b**, Schematic illustration of the neural network architecture used for the classification task. Each of the 784 input neurons, $X^{(j)}$, corresponds to a pixel and is connected to each of the 400 output neurons, $Q^{(k)}$, by a synapse with efficacy, $G^{(jk)}$. A lateral inhibition mechanism is implemented, whereby each output neuron's spike inhibits the rest of the neurons. During training with static unoccluded images (MNIST), standard, i.e. long-term, STDP (LT-STDP) is employed to obtain the fixed weights, \mathbf{W} , in an unsupervised manner. During inference on occluded video (OMNIST), synaptic plasticity switches to ST-STDP. **c**, Comparison between the SNN with and without ST-STDP in terms of the activated output neurons. The 9 most active output neurons over each period of 350 ms are shown. Each neuron is presented as a 2D-map of its fixed weights \mathbf{W} , showing the digit pattern it has been trained to respond to. Colour-coding corresponds to the neuron's count of recorded output spikes over each period. It can be seen that, only when ST-STDP is enabled, a recognized input digit "zero" continues being recognized as such even when it is highly occluded (350-2800 ms, cf. a), and not when it is replaced by noise (2800-3500 ms). **d**, Instantaneous snapshots of the synaptic efficacies of one neuron with ST-STDP from c are shown at every 350-ms instance. **e**, The pre- and post-synaptic spikes corresponding to one synapse for the first 700 ms. The synapse receives input from the upper-most handwritten pixel of this digit. Pre-synaptic spikes cease after 350 ms due to the occlusion. The evolution of its efficacy's short-term component F is also shown in orange.

encoded as binary Poisson processes, e.g. in the context of rate-coding – a principal strategy of input encoding in SNNs^{32,34,48–50} – a temporal dependence in the synaptic update rule, can emerge as part of the algorithm (Supplementary Information, section S6.1). The resulting solution then is an STDP rule, dependent on the time interval τ between the pre- and post-synaptic spikes. Finally, the relaxation dynamics $f(t)$ of the synaptic efficacies towards the resting weights $\mathbf{W}^{(k)}$, e.g. as in Eq. 3, is an expression of STP, thereby fully describing ST-STDP (see Fig. 2b). Note that the dynamics of the bias parameter $G_t^{(0k)}$ captures the evolution of the neuron's intrinsic excitability, a type of use-dependent plasticity that has been observed in numerous experiments.^{51–54}

Remarkably, we show that the model we derived as optimal can be implemented, albeit stochastically, by a network structure and neurons that are also biologically plausible (Supplementary Information, section S6.3). In particular, the soft-max probabilistic inference outputs are computed by stochastic exponential spiking neurons, assembled in a powerful microcircuit structure that is common within neocortical layers,³³ i.e. a soft winner-take-all (WTA) circuit with lateral inhibition.^{32,34,55} Stochastic exponential spiking behaviour is in good agreement with the recorded activity of real neurons.⁵⁶ Using techniques similar to,³² the output spikes of this network can be shown to be samples from the posterior distribution, conditional on the input and its past. The parameter updates of Eq. 2 in this spiking implementation are event-based, they occur at the time of each output spike, and they depend on its latency τ from preceding input spikes. Finally, to complete the biological realism of the model, even the initial, resting weights $\mathbf{W}^{(k)}$ can be obtained through standard long-term STDP³² before the activation of ST-STDP.

An alternative model of a spiking neuron, and a common choice both in computational neuroscience simulations and in neuromor-

phic hardware circuits, owing to its effective simplicity, is the leaky integrate-and-fire (LIF) model. We show for a WTA circuit constructed by LIF neurons, that if it implements elastic clustering through the same ST-STDP rule of equations 1-3, this network also maintains a model of the random continuous environment (Supplementary Information, sections S4, S6).

Application to video recognition

To assess the effectiveness of the ST-STDP-based neural elastic clustering algorithm and its possible influence on cortical computations, we simulate it and apply it on the task of classifying frames of a video of occluded MNIST (OMNIST) handwritten digits (see Methods). New benchmarks and applications, better suited for SNNs, have been highly sought but thus far missing.³⁸ Towards that goal, the task's design here is chosen indeed to specifically demonstrate the strengths of ST-STDP, while being attainable by a single-layer SNN with unsupervised learning and high biological realism. In the OMNIST video, an occluding object progressively hides each digit, and after a random number of frames the digit is fully occluded and replaced by random noise, before the next digit appears in the video (see Fig. 3a). The task is to classify each frame into one of ten digit classes (0-9) or one eleventh class of noisy frames. The MNIST classification task is a standard benchmarking task in which ANNs easily achieve almost perfect accuracies. On the other hand, the derived OMNIST classification task used here is significantly more difficult due to the large occlusions, the noise, and the unpredictable duration of each digit's appearance. We use an SNN of 400 output neurons in a soft-WTA structure consistent with the canonical local connectivity observed in the neocortex,³³ and with the neural implementation we derived for the elastic clustering algorithm. Each neuron is stimulated by rate-coded inputs from 784 pixels through plastic excitatory afferent synapses (see Fig. 3b). The 400 elastic cluster

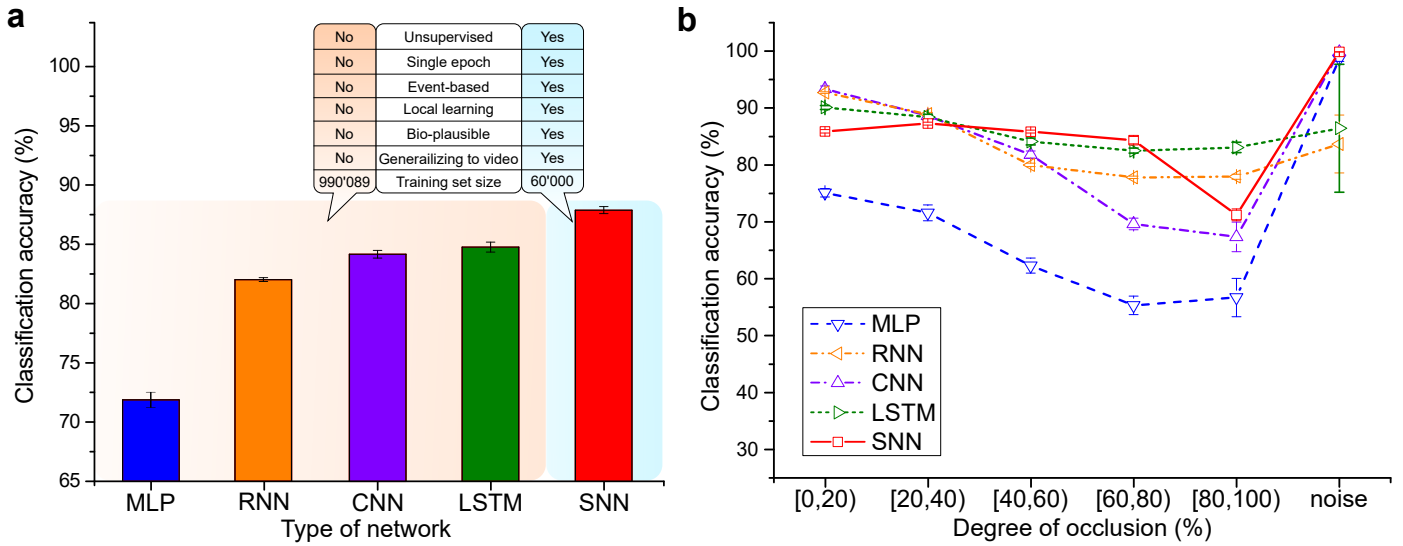


Figure 4: Comparison of SNN and ANN classification results. **a**, Classification accuracy of SNN with ST-STDP on the OMNIST test set compared with that of an MLP, a CNN, an RNN and an LSTM. The SNN is trained on the MNIST training set while the other networks are trained on the OMNIST training set. The bar graph shows the mean and standard deviation over ten runs starting from different random weight initializations. The training set sizes of MNIST and OMNIST are 60,000 and 990,089, respectively. It can be seen that the SNN with ST-STDP achieves higher classification accuracy than all the other networks. In addition, the SNN compares positively across a number of qualities, namely its unsupervised training, in just one epoch, with event-based operation, synaptically-local learning, use of largely biologically-plausible mechanisms, generalization to transforming video from the standard static MNIST images, and from a significantly smaller training set. **b**, The performance of the five models in classifying OMNIST frames with different degrees of occlusion. Also shown is the classification accuracy when a noise frame is presented. Each data point indicates the mean and standard deviation over ten runs starting from different random weight initializations.

neuron-centroids find their resting positions through unsupervised learning that emerges from conventional, long-term STDP,³⁴ and driven by stimulation with the unoccluded MNIST training images. On the MNIST test set, the network achieves a mean classification accuracy of 88.49%. When tested on the OMNIST test set without using ST-STDP or retraining, the performance drops to 61.10%. However, when ST-STDP is enabled at the synapses, we observe that neurons that recognize an input digit continue recognizing it even when it is partly occluded, and without significantly affecting the recognition of subsequent digits or noisy objects (Fig. 3c), reaching a performance of 87.90%. This is achieved as ST-STDP strengthens specifically the synapses that contribute to the recognition of a frame (Fig. 3d-e). The spiking neurons' synaptic vectors follow the input vector and relax to their resting position (Fig. S3) confirming in practice that ST-STDP realizes the theoretical elastic clustering algorithm.

To benchmark the performance of the SNN with ST-STDP, we compare it to the performance of ANNs that we train with backpropagation, specifically a multilayer perceptron (MLP), a convolutional neural network (CNN), a recurrent neural network (RNN), and long short-term memory (LSTM) units, each with at least as many trainable parameters as the SNN (see Methods). The MLP and the CNN generally are well-equipped to tackle tasks of recognizing frames of static images. Indeed, after training on the MNIST training set, they correctly recognize respectively 89.65% and 98.92% of the MNIST testing frames. However, their performance on the OMNIST testing set is significantly lower, i.e. 54.58% and 65.91% respectively, after augmenting the MNIST training set with noisy frames as an additional, 11th class of training images. Their accuracy increases to 71.85% and 84.19% respectively when they are trained on the 990,089 frames of the OMNIST training set (Fig. 4a), which is still lower than the performance of the SNN with ST-STDP, even though the SNN learns

and generalizes from the standard MNIST training set, with no noisy frames or occlusions during training. This advantage stems from the fact that ST-STDP installs a short-term memory in the SNN, which allows it to make use of the relationships between frames, while the CNN and the MLP are not equipped to deal with temporal aspects of data.

On the other hand, the RNN and the LSTM are expected to also exploit the slight temporal regularity present in the OMNIST data, if trained on OMNIST video. However, even these recurrent networks, trained on the full OMNIST training video over multiple epochs, achieve an accuracy of 82.01% and 84.78% which is still lower than the SNN's performance, even though the SNN is only trained on MNIST's 60,000 static images in a single epoch, and in an unsupervised and local manner (Fig. 4a). The SNN's advantage in this case stems partly from the fact that its short-term memory is at the synapse level (see Supplementary Information S9), as opposed to the neuronal-level memory implemented by the recurrency in RNNs and LSTMs. On the one hand, the RNN and the LSTM achieve better accuracy than the SNN in frames with only few visible pixels (Fig. 4b, 80-100% occlusions), due to the persisting neuronal short-term memory of previous frames. On the other hand, this causes a decreased accuracy on subsequently presented noisy frames which are also recognized as digits (Fig. 4b, right-most data-point), falsely, due to the same memory. This has a greater cost on overall accuracy (Fig. 4a), such that the SNN achieves the better trade-off. It is noteworthy that other tasks with more irregular spatiotemporal dynamics, i.e. higher randomness than consistent gradual occlusions, may accentuate this SNN advantage.

Discussion

We have demonstrated theoretically and experimentally that certain properties so far unique to SNNs are optimal for the processing of random but continuous environments, as natural environments

commonly are. This indicates that spike-based operations can provide the brain with statistically optimal internal models of the environment, and may be partly responsible for the brain's computational superiority to machines in interacting with natural environments. We identified short term plasticity as a key mechanism for this theoretical optimality. Moreover, we showed for the first time that the performance of biologically-inspired SNNs can surpass that of ANNs in a certain task, using only spikes and local unsupervised plasticity.

In addition to its biological implications, this algorithm is a new machine-learning approach to modelling dynamic environments, and suggests a category of applications as best addressed by neuromorphic computing. It differs from the currently dominant deep learning techniques for neural AI. Elastic clustering and ST-STDP operate by online adaptation to temporally local information, as opposed to the usual global training with an all-encompassing dataset in a separate prior phase. This partly circumvents a notorious limitation of deep learning, namely that its effectiveness is limited by the breadth and size of the training set. This is demonstrated in our experiments by the SNN's constrained training on only static and untransformed images, and in just one epoch. Furthermore, the SNN's training phase not only is short, but also it does not include examples of the video dynamics. Nevertheless, the SNN outperforms even sophisticated ANNs such as LSTMs, even despite the latter's supervised training on videos. This surprising result is due to the randomness in input changes. Such random dynamics – frequent in nature and exemplified by the video in the experiments – are unlearnable from example sequences in an off-line manner, but are captured by on-line adaptivity.

This adaptivity of neural elastic clustering, combined with the temporal continuity of natural sensory inputs, may have an active role in enabling the CNS to perform robustly even in the presence of only unsupervised and synaptically-local learning, and despite the likely absence of biological analogues to global supervised training based on back-propagation of errors. On the other hand, in machine-learning systems, the advantages of online unsupervised elastic clustering can also be combined with a backpropagation-trained deep SNN or ANN. Specifically, supervised backpropagation training could be used to obtain an initial state of the network, whereas an unsupervised ST-STDP-like scheme could then be used for on-line adaptation to random but continuous transforming environments. These are readily implementable next steps that can apply the strengths of ST-STDP and elastic clustering to larger AI problems, than this first demonstrated application that was purposely constrained by biological plausibility. The results reported here stem from the systematic identification of analogies between biophysics and the spatiotemporal and causal structure of the world. We propose this as a strategy that could reveal more of the principles that optimize the brain for its environment.

References

- [1] Maass, W. Networks of spiking neurons: The third generation of neural network models. *Neural Networks* (1997).
- [2] Ponulak, F. & Kasinski, A. Introduction to spiking neural networks: Information processing, learning and applications. *Acta neurobiologiae experimentalis* **71**, 409–433 (2011).
- [3] Grüning, A. & Bohte, S. M. Spiking neural networks: Principles and challenges. In *Proceedings of European Symposium on Artificial Neural Networks (ESANN)* (2014).
- [4] Brenowitz, S. D. & Regehr, W. G. Associative short-term synaptic plasticity mediated by endocannabinoids. *Neuron* **45**, 419–431 (2005).
- [5] Cassenaer, S. & Laurent, G. Hebbian STDP in mushroom bodies facilitates the synchronous flow of olfactory information in locusts. *Nature* **448**, 709 (2007).
- [6] Erickson, M. A., Maramba, L. A. & Lisman, J. A single brief burst induces glur1-dependent associative short-term potentiation: a potential mechanism for short-term memory. *Journal of cognitive neuroscience* **22**, 2530–2540 (2010).
- [7] Mead, C. Neuromorphic electronic systems. *Proceedings of the IEEE* **78**, 1629–1636 (1990).
- [8] Merolla, P. A. *et al.* A million spiking-neuron integrated circuit with a scalable communication network and interface. *Science* **345**, 668–673 (2014).
- [9] Qiao, N. *et al.* A reconfigurable on-line learning spiking neuromorphic processor comprising 256 neurons and 128k synapses. *Frontiers in neuroscience* **9**, 141 (2015).
- [10] Indiveri, G. & Douglas, R. Neuromorphic networks of spiking neurons. *Nano and Molecular Electronics Handbook* **10** (2018).
- [11] Davies, M. *et al.* Loihi: A neuromorphic manycore processor with on-chip learning. *IEEE Micro* **38**, 82–99 (2018).
- [12] Markram, H., Lübke, J., Frotscher, M. & Sakmann, B. Regulation of synaptic efficacy by coincidence of postsynaptic apss and epsps. *Science* **275**, 213–215 (1997).
- [13] Bi, G.-q. & Poo, M.-m. Synaptic modifications in cultured hippocampal neurons: dependence on spike timing, synaptic strength, and postsynaptic cell type. *Journal of neuroscience* **18**, 10464–10472 (1998).
- [14] Song, S., Miller, K. D. & Abbott, L. F. Competitive hebbian learning through spike-timing-dependent synaptic plasticity. *Nature neuroscience* **3**, 919 (2000).
- [15] Zucker, R. S. Short-term synaptic plasticity. *Annual review of neuroscience* **12**, 13–31 (1989).
- [16] Tsodyks, M. V. & Markram, H. The neural code between neocortical pyramidal neurons depends on neurotransmitter release probability. *Proceedings of the National Academy of Sciences* (1997).
- [17] Chamberlain, S. E., Yang, J. & Jones, R. S. The role of nmda receptor subtypes in short-term plasticity in the rat entorhinal cortex. *Neural plasticity* **2008** (2008).
- [18] Rosenbaum, R., Rubin, J. & Doiron, B. Short term synaptic depression imposes a frequency dependent filter on synaptic information transfer. *PLoS Computational Biology* (2012).
- [19] Moraitis, T., Sebastian, A. & Eleftheriou, E. The role of short-term plasticity in neuromorphic learning: Learning from the timing of rate-varying events with fatiguing spike-timing-dependent plasticity. *IEEE Nanotechnology Magazine* (2018).
- [20] Moraitis, T., Sebastian, A. & Eleftheriou, E. Spiking neural networks enable two-dimensional neurons and unsupervised multi-timescale learning. In *Proceedings of the International Joint Conference on Neural Networks* (2018).
- [21] Boi, F. *et al.* A bidirectional brain-machine interface featuring a neuromorphic hardware decoder. *Frontiers in neuroscience* **10**, 563 (2016).
- [22] Serb, A. *et al.* Memristive synapses connect brain and silicon spiking neurons. *Scientific Reports* **10**, 1–7 (2020).
- [23] Wolpert, D. M., Ghahramani, Z. & Jordan, M. I. An internal model for sensorimotor integration. *Science* **269**, 1880–1882 (1995).
- [24] Körding, K. P. & Wolpert, D. M. Bayesian integration in sensorimotor learning. *Nature* **427**, 244–247 (2004).
- [25] Ma, W. J., Beck, J. M., Latham, P. E. & Pouget, A. Bayesian inference with probabilistic population codes. *Nature neuroscience* **9**, 1432–1438 (2006).
- [26] Blaisdell, A. P., Sawa, K., Leising, K. J. & Waldmann, M. R. Causal reasoning in rats. *Science* **311**, 1020–1022 (2006).
- [27] Griffiths, T. L. & Tenenbaum, J. B. Optimal predictions in everyday cognition. *Psychological science* **17**, 767–773 (2006).
- [28] Doya, K., Ishii, S., Pouget, A. & Rao, R. P. *Bayesian brain: Probabilistic approaches to neural coding* (MIT press, 2007).
- [29] Fiser, J., Berkes, P., Orbán, G. & Lengyel, M. Statistically optimal perception and learning: from behavior to neural representations. *Trends in cognitive sciences* **14**, 119–130 (2010).
- [30] Berkes, P., Orbán, G., Lengyel, M. & Fiser, J. Spontaneous cortical activity reveals hallmarks of an optimal internal model of the environment. *Science* **331**, 83–87 (2011).
- [31] Bastos, A. M. *et al.* Canonical microcircuits for predictive coding. *Neuron* **76**, 695–711 (2012).
- [32] Nessler, B., Pfeiffer, M., Buesing, L. & Maass, W. Bayesian computation emerges in generic cortical microcircuits through spike-timing-dependent plasticity. *PLoS computational biology* **9**, e1003037 (2013).
- [33] Douglas, R. J. & Martin, K. A. Neuronal circuits of the neocortex. *Annual Reviews in Neuroscience* **27**, 419–451 (2004).
- [34] Diehl, P. & Cook, M. Unsupervised learning of digit recognition using spike-timing-dependent plasticity. *Frontiers in Computational Neuroscience* **9**, 99 (2015).
- [35] Poirazi, P., Brannon, T. & Mel, B. W. Pyramidal neuron as two-layer neural network. *Neuron* **37**, 989–999 (2003).
- [36] Gidon, A. *et al.* Dendritic action potentials and computation in human layer 2/3 cortical neurons. *Science* **367**, 83–87 (2020).
- [37] Bellec, G., Salaj, D., Subramoney, A., Legenstein, R. & Maass, W. Long short-term memory and learning-to-learn in networks of spiking neurons. In

- Bengio, S. *et al.* (eds.) *Advances in Neural Information Processing Systems*, 787–797 (Curran Associates, Inc., 2018).
- [38] Pfeiffer, M. & Pfeil, T. Deep learning with spiking neurons: opportunities and challenges. *Frontiers in neuroscience* **12**, 774 (2018).
 - [39] Rajendran, B., Sebastian, A., Schmuker, M., Srinivasa, N. & Eleftheriou, E. Low-power neuromorphic hardware for signal processing applications: A review of architectural and system-level design approaches. *IEEE Signal Processing Magazine* **36**, 97–110 (2019).
 - [40] Woźniak, S., Pantazi, A., Bohnstingl, T. & Eleftheriou, E. Deep learning incorporating biologically inspired neural dynamics and in-memory computing. *Nature Machine Intelligence* **2**, 325–336 (2020).
 - [41] Bengio, Y., Lee, D.-H., Bornschein, J., Mesnard, T. & Lin, Z. Towards biologically plausible deep learning. *arXiv preprint arXiv:1502.04156* (2015).
 - [42] Szatmáry, B. & Izhikevich, E. M. Spike-timing theory of working memory. *PLoS computational biology* **6**, e1000879 (2010).
 - [43] Fiebig, F. & Lansner, A. A spiking working memory model based on hebbian short-term potentiation. *Journal of Neuroscience* **37**, 83–96 (2017).
 - [44] Frey, U., Huang, Y. & Kandel, E. Effects of camp simulate a late stage of ltp in hippocampal ca1 neurons. *Science* **260**, 1661–1664 (1993).
 - [45] Huang, E. P. Synaptic plasticity: going through phases with ltp. *Current Biology* **8**, R350–R352 (1998).
 - [46] Baltaci, S. B., Mogulkoc, R. & Baltaci, A. K. Molecular mechanisms of early and late ltp. *Neurochemical research* **44**, 281–296 (2019).
 - [47] Schiller, J., Major, G., Koester, H. J. & Schiller, Y. Nmda spikes in basal dendrites of cortical pyramidal neurons. *Nature* **404**, 285 (2000).
 - [48] Hubel, D. H. & Wiesel, T. N. Receptive fields of single neurones in the cat’s striate cortex. *The Journal of physiology* **148**, 574–591 (1959).
 - [49] Gerstner, W., Kistler, W. M., Naud, R. & Paninski, L. *Neuronal dynamics: From single neurons to networks and models of cognition* (Cambridge University Press, 2014).
 - [50] Brette, R. Philosophy of the spike: rate-based vs. spike-based theories of the brain. *Frontiers in systems neuroscience* **9**, 151 (2015).
 - [51] Abbott, L. F. & Nelson, S. B. Synaptic plasticity: taming the beast. *Nature neuroscience* **3**, 1178 (2000).
 - [52] Daoudal, G. & Debanne, D. Long-term plasticity of intrinsic excitability: learning rules and mechanisms. *Learning & memory* **10**, 456–465 (2003).
 - [53] Cudmore, R. H. & Turrigiano, G. G. Long-term potentiation of intrinsic excitability in lv visual cortical neurons. *Journal of neurophysiology* **92**, 341–348 (2004).
 - [54] Turrigiano, G. Too many cooks? intrinsic and synaptic homeostatic mechanisms in cortical circuit refinement. *Annual Review of Neuroscience* **34**, 89–103 (2011).
 - [55] Neftci, E. *et al.* Synthesizing cognition in neuromorphic electronic systems. *Proceedings of the National Academy of Sciences* **110**, E3468–E3476 (2013).
 - [56] Jolivet, R., Rauch, A., Lüscher, H.-R. & Gerstner, W. Predicting spike timing of neocortical pyramidal neurons by simple threshold models. *Journal of computational neuroscience* **21**, 35–49 (2006).
 - [57] Cover, T. M. & Thomas, J. A. *Elements of information theory* (John Wiley & Sons, 2012).
 - [58] Diehl, P. & Cook, M. stdp-mnist. <https://github.com/peter-u-diehl/stdp-mnist> (2015).
 - [59] Mitchell, S. J. & Silver, R. A. Shunting inhibition modulates neuronal gain during synaptic excitation. *Neuron* **38**, 433–445 (2003).
 - [60] Ayaz, A. & Chance, F. S. Gain modulation of neuronal responses by subtractive and divisive mechanisms of inhibition. *Journal of neurophysiology* **101**, 958–968 (2009).
 - [61] Wilson, N. R., Runyan, C. A., Wang, F. L. & Sur, M. Division and subtraction by distinct cortical inhibitory networks in vivo. *Nature* **488**, 343 (2012).
 - [62] Amit, D. J. & Tsodyks, M. Quantitative study of attractor neural network retrieving at low spike rates: I. substrate – spikes, rates and neuronal gain. *Network: Computation in neural systems* **2**, 259–273 (1991).

METHODS

Synopsis of the theoretical analysis

Formal definitions and assumptions (see Supplementary Information, section S1), and the remainder of the complete derivation are provided in the Supplementary Information. Here we provide its outline. First, we derive the probability distribution of the data, i.e. of future observations given those of the past, and given the assumptions for continuity and randomness. For this, based on information theory,⁵⁷ we show that the distribution of an object's future observations is a Gaussian centred at its last observation (Fig. 1b, and Supplementary Information, section S2). The combination of this with the stationary unconditional-on-history probability distribution that accounts for the possibility of novel object introductions, composes the probability density function (PDF) of an observed sample conditional on its past. Using the unconditional PDF and Bayes' theorem, the conditional PDF is expressed as a mixture of likelihood functions each attributed to a possible "hidden cause", i.e. label of the observation. Second, we model these functions using distributions that (a) suit the assumptions of the input, (b) are parameterized such that analytical derivation of the optimal parameters is possible by minimizing the Kullback-Leibler divergence of the model from the data, and (c) can be described as neuron activation functions. The derived optimal parameter vectors are determined by the mean values of the likelihood functions. By minimizing the Kullback-Leibler divergence of the model from the data PDF, we show that its components' optimal parameters are given by the means of the data distribution's components (Supplementary Information sections S3, S4). Third, we show that these parameters, as means of distributions, can be regarded as centroids of clusters. In addition, we show that, to optimize the model, these change with each incoming observation, with each inferred posterior, and with time, rendering the parameter optimization interpretable as an online clustering algorithm (Supplementary Information, section S5). Fourth, we extend the model to operate with stochastic measurements of the observations, estimating the value of the underlying variable as a weighted average of past stochastic samples. The weighting of the sample history is derived from the random dynamics of object transformations, and of observed object replacement. This allows the model's optimization algorithm to use spike-based input encoding (Supplementary Information, section S6.1). Fifth, we show that the dynamics of the cluster centroids have in fact the form of short-term Hebbian plasticity, and we show how a neural network with this plasticity can realize this model and its optimization (Supplementary Information section S6.2). Last, we conclude by deriving a fully spike-based machine learning model with spiking outputs, which maintains the sought generative model of the data (Supplementary Information, section S6.3). We derive the results for two models, one based on stochastic exponential and the other based on leaky integrate-and-fire (LIF) neurons.

The OMNIST dataset

The OMNIST testing dataset is a single continuous video derived from the 10,000 images of the MNIST handwritten digit testing dataset. It consists of subsequences, each generated based on an MNIST image. An example of this type of subsequence is shown in Fig. 3a, albeit shortened for the figure, compared to the subsequences of the actual testing and training OMNIST sets. Each MNIST image is shown while an occluding square begins to move vertically, from the top towards the bottom of the frame, and decelerates until it stops at a certain height of the frame. After a random number of frames, the digit and the occlusion disappear and are replaced by a random noisy object that varies between

frames. The noise is generated randomly at each frame, and repeated for four frames. Subsequently, a different MNIST frame is presented, and the process is repeated for all MNIST testing digits, resulting in a video sequence of 164,915 total frames. Similarly, an OMNIST training video, used to train the recurrent ANNs, is derived from the separate set of 60,000 images of the MNIST training dataset, and results in a length of 990,089 frames.

The specific geometry and dynamics of the occlusion and the noise were arbitrarily chosen as follows. Each MNIST frame is repeated for $11 \leq n_f \leq 14$ times, where n_f is randomly and uniformly chosen for each frame. At the first frame for each digit, the square occluding object is located immediately outside the visible part of the square image, so that the first frame of each digit's subsequence is identical to the original MNIST frame. Subsequently, the occluding object begins moving downwards into the frame with a speed of 3 pixels per frame. The occlusion's speed is reduced to 1 pixel per frame when the occlusion is 18 pixels inside the image. When the occlusion reaches 19 pixels, it stops moving until the completion of the sequence of n_f frames for this digit. The noisy object is a rectangle with a width of 15 and a height of 12 pixels, chosen to roughly match the central frame region that the MNIST digits cover. It is generated at each frame as follows. From the 784 pixels of the whole frame, 200 are randomly selected, and, from those, the ones outside the limits of the rectangle are excluded. Each selected pixel is assigned a uniformly random brightness value between 0 and 255.

The dataset's design was chosen to best manifest the strengths of the ST-STDP-enabled SNN, compared to other algorithms, under the constraints of a very simple architecture and training, like our unsupervised WTA. The untransformed dataset must be able to be handled by a single-trained-layer, unsupervised network, thus MNIST was chosen because it fulfils this requirement. While hand-written character recognition using this dataset remains, as demonstrated in the main text, a difficult task for the compared ANNs, this design makes the task achievable by the SNN. Even more difficult, and less arbitrary, datasets could likely be handled by networks combining ST-STDP with more complex architectures. For example, multilayer networks could be trained in a supervised manner, to extract more abstract features than individual pixels, and to recognize patterns in harder training sets than MNIST. On-line adaptivity through ST-STDP could be added subsequently to such a network, during inference on the transforming testing data.

Simulations

SNN structure and operation: The SNN was structured and operated during training according to³⁴ and the associated code in.⁵⁸ Each pixel of the 28x28 input image corresponded to an input neuron firing Poisson spike trains with a rate proportional to the brightness of the pixel. The 784 input neurons were connected through excitatory synapses with 400 output neurons in an all-to-all fashion. In addition, each output neuron was connected to a different inhibitory neuron, and each inhibitory neuron was connected to all other output neurons through inhibitory synapses, implementing lateral inhibition among output neurons. Synapses were conductance-based as opposed to current-based, so each excitatory input spike to a neuron caused the excitatory conductance of the neuron to increase by the corresponding synapse's efficacy, while inhibitory spikes acted on an inhibitory conductance. The conductances decayed exponentially. Each conductance, multiplied by the difference of the neuron's membrane potential from the synapse's resting potential, was added to an excitatory or inhibitory current respectively for excitatory and inhibitory synapses,

and the total current into the neuron changed its membrane potential linearly with time, while the membrane potential also decayed exponentially towards the neuron's resting potential, at all times. Once the neuron's firing threshold was reached, the neuron fired an output spike, and was reset to its reset potential. A refractory period prevented spikes from being produced for a few milliseconds after each output spike.

Deviations of SNN simulations from theory: To test the model, we chose to simulate it by using LIF neurons, which are a convenient model suitable for simulations or implementations with efficient electronic circuits. The theoretically optimal model requires normalized inputs, continuous normalization of the synaptic efficacies, an additional intrinsic neuronal plasticity continuously updating the neuronal threshold, and divisive inhibition in the case of LIF neurons, as opposed to subtractive. Nevertheless, in our simulations we used a simplified model without these particular idealities, using only conventional neuromorphic primitives with the addition of ST-STDP. This demonstrated that ST-STDP itself is powerful, can be robust to the absence of the theoretical idealities, and is thus suitable for simple neuromorphic hardware or simulations. In particular, omitting the additional neuronal memory mechanism that the intrinsic neuronal plasticity would introduce, not only simplified the simulation, but also allowed us to perform a more direct contrast of ST-STDP with other models such as RNNs or LSTMs. These networks also include a decaying neuronal memory, implemented by the self-recurrency, and analogous to an intrinsic neuronal plasticity. Therefore, not including this aspect in the simulated SNN allows us to attribute the demonstrated benefits unambiguously to the plasticity of synapses itself, and to distinguish them from potential advantages due to a sheer diversity of short-term memory mechanisms (neuronal and synaptic).

SNN training: During training, short-term plasticity was not introduced, so the component F of the synaptic efficacy G was inactive, and fixed at zero, and the efficacies were equivalent to the weights W , which were initialized with random values. Each of the 60,000 images from the MNIST training set was input into the network as a 350 ms spike train, followed by a 150 ms resting time. The training set was presented over a single epoch, i.e. only once. Long-term plasticity in the form of STDP was active during training. Weights were depressed when a presynaptic spike followed a postsynaptic one, by an amount proportional to a trace decaying exponentially from the time of the single last postsynaptic spike. Potentiation events were governed by a triplet rule, where a presynaptic spike followed by two postsynaptic spikes caused an increase in the weight proportionally to two traces: one trace decaying exponentially from the time of the last presynaptic spike, and also another trace decaying exponentially from the last postsynaptic spike. At each time step of the training simulation the weights of each neuron were normalized through division by their sum. In addition, a homeostatic mechanism was changing each neuron's intrinsic excitability, through an adaptive threshold increasing every time the neuron fires, and exponentially decaying to its resting value at all times except during the 150 ms resting phases between input presentation. If the presentation of an image produced fewer than five output spikes in total, then the example was repeated with an increased intensity, i.e. by increasing the input firing rates.

SNN testing: To test the performance of the network after its training, we first froze the weights and the firing thresholds. Then we associated each neuron with a label, which was taken to be the label to which the neuron was most responsive across the last presentation of the 60000 training examples. That was the only part where labels were used. Subsequently, we tested the recogni-

tion of the MNIST and the OMNIST testing datasets. In the case of MNIST, each tested image was recognized as belonging to the digit class whose corresponding output neurons had the highest average firing rate during the 350 ms of the image's presentation. Similarly to the training phase, the examples were repeated with increasing intensity until at least five output spikes were produced. For OMNIST, we followed the same testing protocol, but we removed the resting phase between frames, and we did not repeat the frames that caused the network to produce few or no output spikes. This made the implementation ready for future operation with real streaming input, as there was no need to store the data for repetition. The frames that produced no spikes were assigned an 11th inferred label, corresponding to the noisy object of the OMNIST dataset. First we tested the network with ST-STDP turned off, as during training, i.e. with the efficacies G fixed to equal the weights W . Separately, we tested it after enabling ST-STDP, acting on the short-term component F of the efficacies. ST-STDP was implemented as short-term facilitation only, by using a trace each keeping track of the recent presynaptic history. The trace decayed exponentially, and increased with each presynaptic spike. With each postsynaptic spike, the synaptic efficacy increased by an amount, proportional to the value of the trace at that time, by a parameter γ (Eq. 2), which was fixed per synapse and was dependent on the synapse's fixed resting weight W (see Supplementary Information, section S7). Subsequently, the short-term component F decayed exponentially towards zero, and therefore the efficacy G towards its equilibrium value equal to the weight W .

ANN training and testing: The multilayer perceptron (MLP) we used was structured to use one input layer of 784 neurons corresponding to the image pixels, two fully connected hidden layers of 256 sigmoid units each, a layer of 11 sigmoid units, and a final soft-max operation. We trained the network using Adam, using cross entropy as the loss function, with a learning rate of 0.001, and batches of 200 training examples. The training set was shuffled between each full presentation of the set, and 20 epochs reached convergence. The structure of the convolutional network (CNN) comprised a 28x28 input layer, a first convolutional layer computing eight features using a 5x5 filter with ReLU activation, a first max pooling layer with a 2x2 filter and stride of 2, a second convolutional layer of eight features using a 5x5 ReLU filter, a second max pooling layer with a 2x2 filter and stride of 2, a densely connected layer of 400 ReLU neurons and a final dense layer of 11 outputs, passed through a soft-max operation. The network was trained to minimize cross entropy, with gradient descent and dropout (dropout probability of 0.4), with a learning rate of 0.001. The MLP and the CNN were each trained in two separate manners, namely once on the MNIST and once on the OMNIST training set, before testing on the OMNIST testing set. When the 60000 MNIST training images were used for training, the training set was augmented with an additional 11th class of 6000 noisy frames taken from the OMNIST training set. We also trained a fully recurrent neural network (RNN) on the OMNIST training video. The RNN consisted of 784 input neurons, 400 hidden RNN units, fully connected to 11 output units, on which soft-max was applied. To train it, we used gradient descent with a learning rate of 0.001. Training inputs were batches of 128 sequences of a fixed length. The sequences were subsequences from the OMNIST video, and their length was equal to the number of frames of the longest digit's observation, including its subsequent noisy frames, within the OMNIST video, i.e. 21 time steps, i.e. frames. The RNN was stateful, such that the recurrent units' states at the beginning of a batch were those at the end of the previous batch. Each batch was a continuation of the previous one from the OMNIST

video. The sequence of 990089 total training frames was presented twice during training. The minimized loss function was the cross entropy averaged over the 21 time steps of an input sequence. A long short-term memory (LSTM) network was also trained on the same task. The network consisted of 784 inputs, and 90 hidden LSTM cells fully connected to 11 output units on which soft-max was applied. This resulted in a network size of 315990 parameters, slightly larger than the 314000 trained synaptic efficacies and firing thresholds in the SNN of 400 excitatory neurons. The training procedure was the same as for the RNN.

Supplementary Information

S1 Problem formulation and outline of our approach

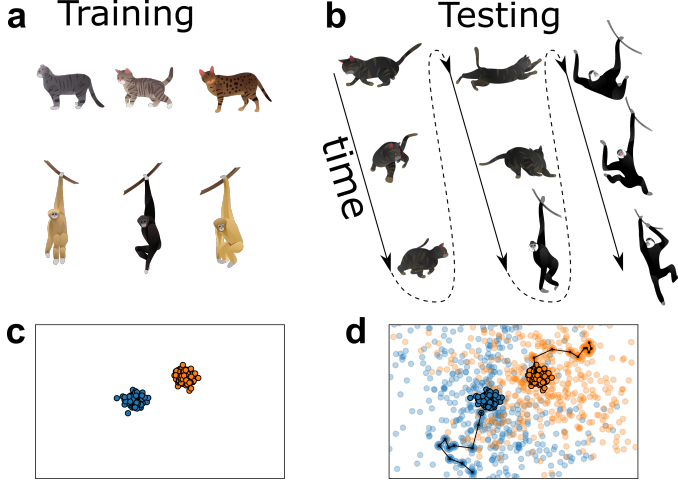


Figure S1: **Schematic depicting the type of problems addressed here.** **a**, Training with typical static examples. **b**, During testing, the environment transforms continuously but randomly. **c**, Training examples may be easily separable and predictable. **d**, Testing patterns are highly unpredictable and non-separable, unless the continuity of objects in time (black line paths) is considered.

We shall describe a quite generic statistical category of spatiotemporal data. Here we first summarize the reasoning, and then we provide mathematical definitions and derivations. The employed data model is a formalization of the postulate that in natural input streams, due to the continuity of natural environments, each instance of the observed input is likely a transformed but similar repetition of a recent instance, unless the observer turns his attention to a different object. The data at each time instance, for example an image of an animal, is associated with a category that is unknown, i.e. a hidden label or "cause", e.g. the animal's species. A training set with typical examples of such objects is available, e.g. frontal images of animals (Fig. S1a, c). After training, each new object that is encountered is typical, from the same distribution as the training set, but is subsequently characterised by temporal dynamics, e.g. animals moving in a field (Fig. S1b, d, Fig. 1a). Because of the continuity of time and space, each observed object is likely to be observed at a point soon after as well, but unlikely to be the one observed at a point far in the future. Each object's properties can change randomly but are continuous in time.

S1.1 Assumptions

Specifically, we make the following assumptions.

1. We model the environment as a set E of I objects: $E = \{iO, \forall i \leq I\}$. For example, the environment may be the images of the MNIST handwritten digit testing dataset, in which case $I = 10,000$, or a room containing three-dimensional objects, or a dictionary of word sounds etc.

2. Each object iO in the environment is associated with a hidden label or "cause" or "class" iC from a finite set of K possible labels, where K is known: $iC \in \{C^{(k)}, \forall k \leq K \in \mathbb{N}\}$. E.g., in the case of the 10 digits of the MNIST dataset, $K = 10$.
3. Each object iO in the environment corresponds at time t to an n -dimensional vector $iO_t \in \mathbb{R}^n$. For example, in the MNIST dataset, objects have $n=784$ dimensions that correspond to the image pixels.
4. Each object vector iO_t undergoes a transformation that is random and has continuous but unknown paths in time, e.g. the transformations due to moving occlusions in the OMNIST dataset.
5. The environment is observed at discrete time points $t \in \{t_1, t_2, \dots, t_T\}$, $T \in \mathbb{N}$. The resulting observation at each time instance t is an n -dimensional vector $X_t \in \mathbb{R}^n$.
6. At each time instance t , exactly one object iO is observed from the environment, be it $O_t = iO$. A stationary Poisson process with a mean rate α triggers changes of the observed object iO into a different one, jO , at random times.
7. An object iO last observed at time t_i , i.e. $O_{t_i} = iO$, is likely to also be observed at time $t > t_i$, i.e. $O_t = O_{t_i}$, with a probability that changes with time $t - t_i$ and ultimately decays to zero. Let A_{t_i} be the event that the object iO last observed at time t_i is also observed at time t . Then, specifically, a decaying function $f(t - t_i)$ determines the odds iP in favour of the observation of the object iO such that:

$$P(A_{t_i}) = \frac{iP}{\sum_{m=1}^I mP} = \frac{f(t - t_i)}{\sum_{m=1}^I mP} \quad (S1)$$

$$\text{and } \lim_{t \rightarrow +\infty} f(t) = 0. \quad (S2)$$

8. At each time instance, the odds that the visible object will be replaced by a novel, previously unseen object, which we call event B are constant and equal to β , i.e.

$$P(B) = \frac{\beta}{\sum_{m=1}^I mP}. \quad (S3)$$

The events B and A_{t_i} for all $1 \leq t_i < t$ cover all possibilities, i.e. either a possible introduction of a novel object or a repetition of one previously observed object. Therefore, from Assumption 8 combined with Assumption 7 it is

$$\sum_{m=1}^I mP = \sum_{i=1}^T f(t - t_i) + \beta. \quad (S4)$$

9. The probability distribution of the novel objects is unknown, but it is independent from the history:

$$p(X_t | B, X_{t_i}, C_{t_j}) = p(X_t | B), \forall i, j : t_i \neq t \neq t_j, \quad (S5)$$

and it is the mixture of the history-independent distributions attributed to each of the K labels $C^{(k)}$:

$$p(X_t | B) = \sum_{k=1}^K p(X_t | C_t^{(k)}, B) P(C_t^{(k)} | B). \quad (S6)$$

The task of the observer, i.e. the machine learning problem that is addressed (Fig. 1a, Fig. S1), is to maintain an up-to-date generative model of future observations, given the past ones, under the Assumptions 1-9 stated above.

S1.2 Sketch of the derivation

First, based on the assumptions, we derive the probability distribution of future observations given the past ones, which has two components, one conditional on the past, and one unconditional, i.e. independent, probability distribution component describing introductions of novel objects. The history-dependent part is derived conditional on the history of past observations and of past posterior probabilities that infer the hidden class label. Using this distribution and Bayes' theorem we also get the analytical form of posterior probability for each class given one observation, its history, and past posteriors. These past posterior probabilities, however, are still unknown. To estimate them, we formulate a parameterized generative mixture model of the probability distribution, and we find the analytical form of its optimal parameters given the past inputs, i.e. the parameters that minimize the cross-entropy between the model and the data. The result is that the optimal parameter vector of each component of the mixture model is determined by the mean of each component of the data distribution. These parameters can be therefore regarded as centroids of clusters, with positions that change with each new observation and with time, and we describe this derived novel clustering algorithm. We notice that the dynamics of the cluster centroids are in fact identical to short-term Hebbian plasticity, and we show how a neural network with this plasticity can realize this optimal clustering. Lastly, we extend the model to operate with stochastic measurements of the observations, which allows the algorithm to use spike-based input encoding, and we conclude by deriving a fully spike-based machine-learning model, i.e. with spiking outputs too, that maintains the sought generative model of the data.

S2 The probability distribution of the data

Let $\mathbf{X}_t = \mathbf{X}_{T+1}$ be the $T+1^{\text{st}}$ sample observed at time $t = t_{T+1} > t_T$, and its associated hidden label be $C_t = C_{T+1}$. Let \mathcal{X}_t be the sequence of the samples preceding \mathbf{X}_t . Let \mathcal{C}_t be a sequence of random variables, such that these random variables represent the conditional probabilities $P(C_{t_i}^{(k)} | \mathbf{X}_{t_i}, \mathcal{X}_{t_i}, \mathcal{C}_{t_i}), \forall i: t_1 < t_i < t$, of the hidden labels preceding C_t , where $C_t^{(k)}$ is the event that the hidden label of the observation at time t is $C^{(k)}$. In case the label of the observation were known to be $C^{(k)}$, then $P(C_{t_i}^{(k)} | \mathbf{X}_{t_i}, \mathcal{X}_{t_i}, \mathcal{C}_{t_i}) = 1$ and $P(C_{t_i}^{(j)} | \mathbf{X}_{t_i}, \mathcal{X}_{t_i}, \mathcal{C}_{t_i}) = 0, \forall j \neq k$. Importantly, this way of referring to the labels allows us to apply it also to labels that are hidden, due to its probabilistic form. It is also practical for the derivation of the statistical model of the data in the next section.

Theorem S2.1. *Given the history \mathcal{X}_t and \mathcal{C}_t of a future sample \mathbf{X}_t , the probability distribution of this sample is*

$$p(\mathbf{X}_t | \mathcal{X}_t, \mathcal{C}_t) = \frac{1}{\sum_{i=1}^T f(t-t_i) + \beta} \cdot \sum_{k=1}^K \sum_{i=1}^T \left[\mathcal{N}(\mathbf{X}_{t_i}, \mathbf{\Sigma}_{t_i,t}) P(C_{t_i}^{(k)} | \mathbf{X}_{t_i}, \mathcal{X}_{t_i}, \mathcal{C}_{t_i}) f(t-t_i) + \beta p(\mathbf{X}_t | C_t^{(k)}, B) P(C_t^{(k)} | B) \right], \quad (\text{S7})$$

where $\mathcal{N}(\mathbf{X}_{t_i}, \mathbf{\Sigma}_{t_i,t})$ is a normal distribution centred at \mathbf{X}_{t_i} , and with a covariance matrix $\mathbf{\Sigma}_{t_i,t}$ that depends on the time interval $t - t_i$.

Proof.

$$p(\mathbf{X}_t | \mathcal{X}_t, \mathcal{C}_t) = \sum_{i=1}^T p(\mathbf{X}_t | \mathcal{X}_t, \mathcal{C}_t, A_{t_i}) P(A_{t_i}) + p(\mathbf{X}_t | \mathcal{X}_t, \mathcal{C}_t, B) P(B) = \frac{\sum_{i=1}^T p(\mathbf{X}_t | \mathcal{X}_t, \mathcal{C}_t, A_{t_i}) f(t-t_i) + p(\mathbf{X}_t | B) \beta}{\sum_{i=1}^T f(t-t_i) + \beta} \quad (\text{S8})$$

The second term $p(\mathbf{X}_t | B)$ is the unconditional-on-history probability which is fixed and independent of time or history, as assumed in Section S1.1, Assumption 9. We aim to expand the first term also as a function of the known assumptions and of the visible aspects of the data. We decompose this distribution into the mixture of its K classes:

$$\sum_{i=1}^T p(\mathbf{X}_t | \mathcal{X}_t, \mathcal{C}_t, A_{t_i}) f(t-t_i) = \sum_{k=1}^K \sum_{i=1}^T p(\mathbf{X}_t | C_t^{(k)}, \mathcal{X}_t, \mathcal{C}_t, A_{t_i}) P(C_t^{(k)} | \mathcal{X}_t, \mathcal{C}_t, A_{t_i}) \cdot f(t-t_i). \quad (\text{S9})$$

The first term of the product in Eq. S9 is

$$p(\mathbf{X}_t | C_t^{(k)}, \mathcal{X}_t, \mathcal{C}_t, A_{t_i}) = p(\mathbf{X}_t | \mathcal{X}_t, A_{t_i}), \quad (\text{S10})$$

because the probability distribution of the new sample in event A_{t_i} depends only on the past samples, not the labels.

In addition, the second term in Eq. S9, due to the definition of A_{t_i} , is

$$P(C_t^{(k)} | \mathcal{X}_t, \mathcal{C}_t, A_{t_i}) = P(C_t^{(k)} | \mathcal{X}_{t_i}, \mathcal{C}_{t_i}, A_{t_i}). \quad (\text{S11})$$

We will be using $P_{t_i}(C^k) := P(C_t^{(k)} | \mathcal{X}_{t_i}, \mathcal{C}_{t_i}, A_{t_i})$ as the short-hand form of $P(C_t^{(k)} | \mathcal{X}_{t_i}, \mathcal{C}_{t_i}, A_{t_i})$.

In a key step, through assumption 4 we derive a prior belief about the expected distribution of the increments of an object $j\mathbf{O}$ as a function of time, from the object's random but continuous dynamics. In the absence of additional information, the increment $\delta_j \mathbf{O}_{t_i,t} = j\mathbf{O}_t - j\mathbf{O}_{t_i}$ is unbiased, i.e. the mean of its distribution is zero. The temporal continuity of the objects implies that the variance of this distribution increases with time and at each point in time it is specified. Based on this, the maximum-entropy estimate probability distribution of this increment is a Gaussian.⁵⁷ Therefore, according to the principle of maximum entropy, this Gaussian is the best estimate for the distribution. Taken together, these imply that, in expectation, the dynamics of each object are a Wiener process, which can be used as a Mean Field Approximation of the objects' dynamics. The Wiener process that governs the evolution of the objects implies that a Wiener process also describes the evolution of the object's observed features \mathbf{X}_t between two observations. Therefore, A_{t_i} , i.e. knowing that the object at time t was last observed at time t_i , implies:

$$A_{t_i} \implies \mathbf{X}_t \sim \mathcal{N}(\mathbf{X}_{t_i}, \mathbf{\Sigma}_{t_i,t}), \quad (\text{S12})$$

where $\mathcal{N}(\mathbf{X}_{t_i}, \mathbf{\Sigma}_{t_i,t})$ is a normal distribution centred at \mathbf{X}_{t_i} , and with a covariance matrix that depends on $t - t_i$. By using Eq. S11 and Eq. S12, Eq. S9 becomes

$$\sum_{i=1}^T p(\mathbf{X}_t | \mathcal{X}_t, \mathcal{C}_t, A_{t_i}) f(t-t_i) = \sum_{k=1}^K \sum_{i=1}^T \mathcal{N}(\mathbf{X}_{t_i}, \mathbf{\Sigma}_{t_i,t}) P_{t_i}(C^k) f(t-t_i). \quad (\text{S13})$$

By using Eq. S13 and Eq. S6, Eq. S8 proves the theorem. ■

Theorem S2.1 yields a distribution, which, given past observations \mathbf{X}_{t_i} , past labels C_{t_i} , as well as distributions $\mathcal{N}(\mathbf{X}_{t_i}, \mathbf{\Sigma}_{t_i,t})$ and $p(\mathbf{X}_t | C_t^{(k)})$, can generate new samples \mathbf{X}_t from the actual data. On the other hand, through the same distribution, for any given

sample and its history one can infer the probabilities associated with each possible hidden label of the sample.

Theorem S2.2. *For any given sample \mathbf{X}_t , and history \mathcal{X}_t and \mathcal{C}_t , the probabilities associated with each possible value $C^{(k)}$ of the hidden class label C_t that led to the generation of the observation are inferred as*

$$P(C_t^{(k)}|\mathbf{X}_t, \mathcal{X}_t, \mathcal{C}_t) = \frac{p(\mathbf{X}_t, C_t^{(k)}|\mathcal{X}_t, \mathcal{C}_t)}{\sum_{l=1}^K p(\mathbf{X}_t, C_t^{(l)}|\mathcal{X}_t, \mathcal{C}_t)}, \quad (\text{S14})$$

$$\begin{aligned} \text{where } p(\mathbf{X}_t, C_t^{(k)}|\mathcal{X}_t, \mathcal{C}_t) \\ = \frac{1}{\sum_{i=1}^T f(t-t_i) + \beta} \cdot \sum_{i=1}^T \left[\mathcal{N}(\mathbf{X}_{t_i}, \boldsymbol{\Sigma}_{t_i, t}) P_{t_i}(C^{(k)}) f(t-t_i) \right. \\ \left. + \beta p(\mathbf{X}_t|C_t^{(k)}, B) P(C_t^{(k)}|B) \right]. \quad (\text{S15}) \end{aligned}$$

This is easily shown through Bayes' theorem applied to the distribution of Eq. S7. But, to compute $p(\mathbf{X}_t|\mathcal{X}_t, \mathcal{C}_t)$ and $P(C_t^{(k)}|\mathbf{X}_t, \mathcal{X}_t, \mathcal{C}_t)$ with Eq. S7 and Eq. S14, the past probabilities $P_{t_i}(C^{(k)})$ are needed and are unknown. To estimate these, we will make a parametrized model of the data distribution, and find its parameters such that it is as similar as possible to the real distribution.

S3 Modelling the data with a mixture of exponentials

S3.1 The mixture model and its optimal parameters

Definition S3.1. *Consider a mixture model distribution q : $q(\mathbf{X}_t) = \sum_{k=1}^K q(\mathbf{X}_t|C_t^{(k)}) Q(C_t^{(k)})$, approximating some data distribution p that is also a mixture of K components. We choose a mixture of exponentials and we parametrize $Q(C_t^{(k)}; G_0^{(k)})$ also as an exponential, specifically:*

$$q(\mathbf{X}_t^{(j)}|C_t^{(k)}; G^{(jk)}) = e^{G^{(jk)} \cdot \frac{\mathbf{X}_{jt}}{\|\mathbf{X}_t\|}}, \forall j > 0, k \quad (\text{S16})$$

$$Q(C_t^{(k)}; G_0^{(k)}) = e^{G_0^{(k)}}, \forall k. \quad (\text{S17})$$

In addition, the parameter vectors are subject to the normalization constraints: $\|\mathbf{G}^{(k)}\| = 1, \forall k$, and $\sum_{k=1}^K e^{G_0^{(k)}} = 1$.

Assuming that the dimensions $\mathbf{X}_t^{(j)}$ of the observed variable \mathbf{X}_t are conditionally independent from each other, then $p(\mathbf{X}_t) = \prod_{j=1}^n p(\mathbf{X}_t^{(j)})$, so the model we have chosen is a reasonable choice because it factorizes similarly:

$$\begin{aligned} q^{(k)} &:= q(\mathbf{X}_t|C_t^{(k)}; \mathbf{G}^{(k)}) = \prod_{j=1}^n q(\mathbf{X}_t^{(j)}|C_t^{(k)}; G^{(jk)}) = \\ &= e^{\sum_{j=1}^n G^{(jk)} \frac{\mathbf{X}_{jt}}{\|\mathbf{X}_t\|}} = e^{u_t^{(k)}}, \text{ where } u_t^{(k)} = \frac{\mathbf{G}^{(k)} \cdot \mathbf{X}_t}{\|\mathbf{G}^{(k)}\| \cdot \|\mathbf{X}_t\|}, \text{ i.e. the cosine similarity of the two vectors.} \end{aligned}$$

Theorem S3.1. *The optimal parameters of such a mixture model are*

$$\text{opt } G_0^{(k)} = \ln P(C_t^{(k)}) \quad (\text{S18})$$

$$\text{and } \text{opt } \mathbf{G}^{*(k)} = \frac{\text{opt } \mathbf{G}^{(k)}}{\|\text{opt } \mathbf{G}^{(k)}\|} = \frac{E_{p^{(k)}}[\mathbf{X}_t]}{\|E_{p^{(k)}}[\mathbf{X}_t]\|}, \quad (\text{S19})$$

$$\text{where } \text{opt } \mathbf{G}^{(k)} = c \cdot E_{p^{(k)}}[\mathbf{X}_t], c \in \mathbb{R}, \quad (\text{S20})$$

$$\text{and } p^{(k)} := p(\mathbf{X}_t|C_t^{(k)}) \quad (\text{S21})$$

for every k .

Proof. The model q is optimal from a minimum cross-entropy perspective if its parameters equal those parameters $\mathbf{G} = \text{opt } \mathbf{G}$ that minimize the model's Kullback-Leibler divergence with the data distribution p . $D_{KL}(p(\mathbf{X}_t)||q(\mathbf{X}_t; \mathbf{G}))$. Because $p^{(k)} := p(\mathbf{X}_t|C_t^{(k)})$ is independent from $p^{(l)}$, and $q^{(k)} := q(\mathbf{X}_t|C_t^{(k)}; \mathbf{G}^{(k)})$ is independent from $\mathbf{G}^{(l)}$ for every $l \neq k$, we can find the set of parameters that minimize the KL divergence of the mixtures, by minimizing the KL divergence of each component k : $\min D_{KL}(p^{(k)}||q^{(k)}), \forall k$, and simultaneously setting $P(C_t^{(k)}) = Q(C_t^{(k)}; G_0^{(k)})$, $\forall k$.

From Eq. S17 and this last condition, Eq. S18 of the Theorem can be proven. Further,

$$\begin{aligned} \text{opt } \mathbf{G}^{(k)} &:= \arg \min_{\mathbf{G}^{(k)}} D_{KL}(p^{(k)}||q^{(k)}) \\ &= \arg \min_{\mathbf{G}^{(k)}} \int_{\mathbf{X}_t} p^{(k)} \ln \frac{p^{(k)}}{q^{(k)}} d\mathbf{X}_t \\ &= \arg \max_{\mathbf{G}^{(k)}} E_{p^{(k)}}[u_t^{(k)}]. \quad (\text{S22}) \end{aligned}$$

This follows from using the definition of $q^{(k)}$, and it is the expected value of the cosine similarity $u_t^{(k)}$. Due to the symmetry of the cosine similarity, it follows that

$$\begin{aligned} \text{opt } \mathbf{G}^{(k)} &= \arg \max_{\mathbf{G}^{(k)}} \cos(\mathbf{G}^{(k)}, E_{p^{(k)}}[\mathbf{X}_t]) \\ &= c \cdot E_{p^{(k)}}[\mathbf{X}_t], c \in \mathbb{R}. \quad (\text{S23}) \end{aligned}$$

Enforcement of the requirement for normalization of the vector leads to the unique solution $\text{opt } \mathbf{G}^{*(k)}$. ■

S3.2 The optimal parameters given the history of observations

We will now further specify this solution, for the specific distribution $p(\mathbf{X}_t|\mathcal{X}_t, \mathcal{C}_t)$ as described in Eq. S7, and its components $p^{(k)}(\mathbf{X}_t|\mathcal{X}_t, \mathcal{C}_t)$.

Theorem S3.2. *Let it be $\mathbf{W} := E_{p^{(k)}}[\mathbf{X}_t]$, and $e^{W_0^{(k)}} := P(C_t^{(k)}|B)$. The optimal parameters of the model of Definition S3.1, for data following the assumptions of paragraph S1.1, are, for each component k ,*

$$\text{opt } \mathbf{G}_t^{(k)} = \frac{1}{\beta e^{W_0^{(k)}}} \sum_{i=1}^T \mathbf{X}_{t_i} Q_{t_i}(C^{(k)}) f(t-t_i) + \mathbf{W} \quad (\text{S24})$$

$$e^{G_{0t}^{(k)}} = \frac{\sum_{i=1}^T Q_{t_i}(C^{(k)}) f(t-t_i) + e^{W_0^{(k)}} \beta}{\sum_{i=1}^T f(t-t_i) + \beta}, \quad (\text{S25})$$

$$\text{where } Q_t(C^{(k)}) = \frac{e^{u_t^{(k)} + G_{0t}^{(k)}}}{\sum_{l=1}^K e^{u_t^{(l)} + G_{0t}^{(l)}}}. \quad (\text{S26})$$

Proof.

$$p(\mathbf{X}_t|\mathcal{X}_t, \mathcal{C}_t) = \sum_{k=1}^K p^{(k)}(\mathbf{X}_t|\mathcal{X}_t, \mathcal{C}_t) \cdot P(C_t^{(k)}|\mathcal{X}_t, \mathcal{C}_t), \quad (\text{S27})$$

and in conjunction with the alternative expression of $p(\mathbf{X}_t|\mathcal{X}_t, \mathcal{C}_t)$ in Eq. S7, it follows that

$$\begin{aligned} p^{(k)}(\mathbf{X}_t|\mathcal{X}_t, \mathcal{C}_t) \cdot P(C_t^{(k)}|\mathcal{X}_t, \mathcal{C}_t) &= \frac{1}{\sum_{i=1}^T f(t-t_i) + \beta} \\ &\cdot \sum_{i=1}^T \left[\mathcal{N}(\mathbf{X}_{t_i}, \boldsymbol{\Sigma}_{t_i, t}) P_{t_i}(C^{(k)}) f(t-t_i) + \beta p(\mathbf{X}_t|C_t^{(k)}, B) P(C_t^{(k)}|B) \right] \quad (\text{S28}) \end{aligned}$$

assuming $P(C_t^{(k)}|\mathcal{X}_t, \mathcal{C}_t) \neq 0$. In this Eq., $P(C_t^{(k)}|\mathcal{X}_t, \mathcal{C}_t)$ is still unknown. But it is

$$P(C_t^{(k)} | \mathcal{X}_t, \mathcal{C}_t) = \frac{\sum_{i=1}^T P(C_{t_i}^{(k)} | \mathbf{X}_{t_i}, \mathcal{X}_{t_i}, \mathcal{C}_{t_i}) f(t - t_i) + \beta P(C_t^{(k)} | B)}{\sum_i f(t - t_i) + \beta}, \quad (\text{S29})$$

therefore

$$p_t^{(k)} = \frac{1}{Z_t^{(k)}} \sum_{i=1}^T \left[\mathcal{N}(\mathbf{X}_{t_i}, \boldsymbol{\Sigma}_{t_i,t}) P(C_{t_i}^{(k)} | \mathbf{X}_{t_i}, \mathcal{X}_{t_i}, \mathcal{C}_{t_i}) f(t - t_i) + \beta p(\mathbf{X}_t | C_t^{(k)}, B) P(C_t^{(k)} | B) \right], \quad (\text{S30})$$

where $Z_t^{(k)}$ is the appropriate normalization factor. $P(C_{t_i}^{(k)} | \mathbf{X}_{t_i}, \mathcal{X}_{t_i}, \mathcal{C}_{t_i})$ are missing, but can be estimated by the model as

$$Q_t(C^{(k)}) := Q(C_t^{(k)} | \mathbf{X}_t; {}^{n+1}\mathbf{G}_t^{(k)}), \quad (\text{S31})$$

where ${}^{n+1}\mathbf{G}_t^{(k)} = (G_t^{(jk)}, j = 0 \dots n)$ if its optimal parameters are known. For this, we derive the analytical form of $Q_t(C^{(k)})$. It is

$$q(\mathbf{X}_t; {}^{n+1}\mathbf{G}_t) = \sum_{k=1}^K q(\mathbf{X}_t | C_t^{(k)}; \mathbf{G}_t^{(k)}) Q(C_t^{(k)}; G_{0t}^{(k)}) = \sum_{k=1}^K e^{u_t^{(k)} + G_{0t}^{(k)}} \quad (\text{S32})$$

and thus from Bayes' rule we arrive at Eq. S26. Using this estimate $Q_t(C^{(k)})$, and the fact that $E_{\mathcal{N}(\mathbf{x}_{t_i}, \boldsymbol{\Sigma}_{t_i,t})}[\mathbf{X}_t] = \mathbf{X}_{t_i}$ we compute $E_{p_t^{(k)}}[\mathbf{X}_t]$ from Eq. S30, and thus the optimal (un-normalized) parameter vector ${}_{opt}\mathbf{G}^{(k)}$ for every k and t with Eq. S37, proving Eq. S24. Lastly, through Eq. S18 we find $e^{G_{0t}^{(k)}}$ as well. ■

For $t = t_1$, the optimal estimate of $P_1(C^{(k)})$ is $Q(C_1^{(k)} | \mathbf{X}_1; {}^{n+1}\mathbf{G}_1^{(k)})$, where $G_1^{(jk)} = W_1^{(jk)}$. Using this first estimate, iteratively we can calculate the subsequent optimal parameters ${}_{opt}\mathbf{G}_t^{(k)}$ and ${}_{opt}G_{0t}^{(k)}$, and probabilities $Q_t(C^{(k)})$. \mathbf{W} and $\mathbf{W}_0^{(k)}$ themselves can both be estimated with a standard technique such as Expectation-Maximization (EM), using samples from distribution $p(\mathbf{X}_t | B)$.

S4 Modelling the data with a linear mixture

S4.1 The mixture model and its optimal parameters

Definition S4.1. Consider a mixture model distribution q : $q(\mathbf{X}_t) = \sum_{k=1}^K q(\mathbf{X}_t | C_t^{(k)}) Q(C_t^{(k)})$, approximating some data distribution p that is also a mixture of K components. We choose a mixture of piecewise linear likelihood functions, specifically:

$$q^{(k)} := q(\mathbf{X}_t | C_t^{(k)}; \mathbf{G}^{(k)}) = \frac{1}{Z} \max(u_t^{(k)}, 0) \quad (\text{S33})$$

where Z is a normalization factor, and $u_t^{(k)} = \frac{\mathbf{G}^{(k)} \cdot \mathbf{X}_t}{\|\mathbf{G}^{(k)}\| \cdot \|\mathbf{X}_t\|}$, i.e. the cosine similarity of the two vectors $\mathbf{G}^{(k)}$ and \mathbf{X}_t . The joint probability is

$$q(\mathbf{X}_t, C_t^{(k)}) \equiv q(\mathbf{X}_t | C_t^{(k)}) Q(C_t^{(k)}) = \max\left(\frac{u_t^{(k)}}{Z}, 0\right) Q(C_t^{(k)}) \quad (\text{S34})$$

and the parametrized model approximates it as

$$q(\mathbf{X}_t, C_t^{(k)}; {}^{n+1}\mathbf{G}_t^{(k)}) \approx \max\left(\frac{u_t^{(k)} + G_{0t}^{(k)}}{Z}, 0\right). \quad (\text{S35})$$

In addition, the parameter vectors are subject to the normalization constraints: $\|\mathbf{G}^{(k)}\| = 1, \forall k$, and $\sum_{k=1}^K e^{G_0^{(k)}} = 1$.

Theorem S4.1. The optimal parameters of such a mixture model are

$${}_{opt}\mathbf{G}^{*(k)} = \frac{{}_{opt}\mathbf{G}^{(k)}}{\|{}_{opt}\mathbf{G}^{(k)}\|} = \frac{E_{p^{(k)}}[\mathbf{X}_t]}{\|E_{p^{(k)}}[\mathbf{X}_t]\|}, \quad (\text{S36})$$

$$\text{where } {}_{opt}\mathbf{G}^{(k)} = c \cdot E_{p^{(k)}}[\mathbf{X}_t], c \in \mathbb{R}, \quad (\text{S37})$$

$$p^{(k)} := p(\mathbf{X}_t | C_t^{(k)}) \quad (\text{S38})$$

for every k and the bias parameter of each component k is related to $P(C_t^{(k)})$ as

$$\begin{aligned} &\iff P(C_t^{(k)}) \\ &= \sqrt{1 - (G_0^{(k)})^2} + G_0^{(k)} \arccos(-G_0^{(k)}). \end{aligned} \quad (\text{S39})$$

and can be approximated as

$${}_{opt}G_0^{(k)} = P(C_t^{(k)}) - 1 \quad (\text{S40})$$

for every k .

Proof. The model is optimal from a minimum cross-entropy perspective if its parameters equal those parameters $\mathbf{G} = {}_{opt}\mathbf{G}$ that minimize the Kullback-Leibler divergence between the mixture distributions p and q :

$$\min D_{KL}(p(\mathbf{X}_t) || q(\mathbf{X}_t | \mathbf{G}^*)). \quad (\text{S41})$$

Because $p^{(k)} := p(\mathbf{X}_t | C_t^{(k)})$ is independent from $p^{(l)}$, and $q^{(k)} := q(\mathbf{X}_t | C_t^{(k)}, \mathbf{G}^{(k)})$ is independent from $\mathbf{G}^{(l)}$ for every $l \neq k$, we can find the set of parameters that minimize the KL divergence of the mixtures, by minimizing the KL divergence of each component k :

$$\min D_{KL}(p^{(k)} || q^{(k)}), \forall k. \quad (\text{S42})$$

As in Theorem S3.1, it follows that

$${}_{opt}\mathbf{G}^{(k)} = \arg \max E_{p^{(k)}}[\ln q^{(k)}]. \quad (\text{S43})$$

The parameter vectors that bring this expected value to a (local) maximum are found by demanding that its derivative equal zero:

$$\frac{\partial E_{p^{(k)}}[\ln q^{(k)}]}{\partial \mathbf{G}^{(k)}} = 0. \quad (\text{S44})$$

Each vector $\mathbf{G}^{(k)}$ defines a unique angle $\phi_0^{(k)}$ with the fixed vector $E_{p^{(k)}}[\mathbf{X}_t]$:

$$\phi_0^{(k)} = \angle(\mathbf{G}^{(k)}, E_{p^{(k)}}[\mathbf{X}_t]). \quad (\text{S45})$$

Therefore, equivalently to Eq. S44, but using this uniquely corresponding angle instead of $\mathbf{G}^{(k)}$, we can demand that

$$\frac{\partial E_{p^{(k)}}[\ln q^{(k)}]}{\partial \phi_0^{(k)}} = 0. \quad (\text{S46})$$

But $q^{(k)}$ is defined based on the cosine similarity $u^{(k)}$ that is the cosine of an angle different from $\phi_0^{(k)}$. In particular, it is the cosine of

$$\phi^{(k)} := \angle(\mathbf{G}^{(k)}, \mathbf{X}_t). \quad (\text{S47})$$

To find the solution of S46, we will express $q^{(k)}$ with respect to $\phi_0^{(k)}$. Let $\theta^{(k)}$ be such that

$$\phi^{(k)} = \phi_0^{(k)} + \theta^{(k)}. \quad (\text{S48})$$

From the definition of the model, it is

$$\begin{aligned} q^{(k)} &= \frac{1}{Z} \max(\cos \phi^{(k)}, 0) \\ &= \frac{1}{Z} \max(\cos(\phi_0^{(k)} + \theta^{(k)}), 0). \end{aligned} \quad (\text{S49})$$

The normalization factor Z can be found as follows.

$$\int_0^{2\pi} q^{(k)} d\phi^{(k)} = 1 \iff \quad (\text{S50})$$

$$\int_0^{2\pi} \frac{1}{Z} \max(\cos \phi^{(k)}, 0) d\phi^{(k)} = 1 \iff \quad (\text{S51})$$

$$Z = \int_0^{\pi/2} \cos \phi^{(k)} d\phi^{(k)} + \int_{3\pi/2}^{2\pi} \cos \phi^{(k)} d\phi^{(k)} = 2, \quad (\text{S52})$$

i.e.

$$q^{(k)} = \frac{1}{2} \max(\cos \phi^{(k)}, 0) \\ = \frac{1}{2} \max(\cos(\phi_0^{(k)} + \theta^{(k)}), 0). \quad (\text{S53})$$

Using this form we will find the optimal angle $_{opt}\phi_0^{(k)}$ from Eq. S46. For $\pi/2 < \phi^{(k)} < 3\pi/2$, Eq. S46 is true for any $\phi_0^{(k)}$. For $0 \leq \phi^{(k)} \leq \pi/2$ or $3\pi/2 \leq \phi^{(k)} \leq 2\pi$, it is

$$E_{p^{(k)}} \left[\frac{1}{q^{(k)}} \frac{\partial q^{(k)}}{\partial \phi_0^{(k)}} \right] = 0 \iff \quad (\text{S54})$$

$$E_{p^{(k)}} \left[\frac{1}{q^{(k)}} \frac{\partial \cos(\phi^{(k)})}{\partial \phi_0^{(k)}} \right] = 0 \iff \quad (\text{S55})$$

$$E_{p^{(k)}} \left[\frac{1}{q^{(k)}} (-\sin \phi^{(k)}) \right] = 0 \iff \quad (\text{S56})$$

$$E_{p^{(k)}} [\sin \phi^{(k)}] = 0 \iff \quad (\text{S57})$$

$$E_{p^{(k)}} [\phi^{(k)}] = 0. \quad (\text{S58})$$

We will now show that $\phi_0^{(k)} = 0$ is a solution that satisfies this condition. If $\phi_0^{(k)} = 0$, i.e. $\angle(\mathbf{G}^{(k)}, E_{p^{(k)}}[\mathbf{X}_t]) = 0$, then

$$\phi^{(k)} = \angle(\mathbf{G}^{(k)}, \mathbf{X}_t) = \angle(E_{p^{(k)}}[\mathbf{X}_t], \mathbf{X}_t). \quad (\text{S59})$$

Also, from Eq. S48, it follows that $\theta^{(k)} = \phi^{(k)}$, because $\phi_0^{(k)} = 0$. Therefore,

$$\theta^{(k)} = \angle(E_{p^{(k)}}[\mathbf{X}_t], \mathbf{X}_t) \\ \implies E_{p^{(k)}} [\theta^{(k)}] = \angle(E_{p^{(k)}}[\mathbf{X}_t], E_{p^{(k)}}[\mathbf{X}_t]) = 0. \quad (\text{S60})$$

From Eq. S48, and using Eq. S60 and our assumption that $\phi_0^{(k)} = 0$, it follows that $E_{p^{(k)}} [\phi^{(k)}] = E_{p^{(k)}} [\phi_0^{(k)}] + E_{p^{(k)}} [\theta^{(k)}] = 0$, and this is Eq. S58. Therefore $\phi_0^{(k)} = 0$ is indeed a solution that satisfies the condition of Eq. S58.

Because the optimal parameter vector $_{opt}^n \mathbf{G}^{(k)}$ satisfies this condition, then, from the definition of $\phi_0^{(k)}$ in Eq. S45, it follows that

$$_{opt}^n \mathbf{G}^{(k)} = c E_{p^{(k)}} [\mathbf{X}_t] \quad (\text{S61})$$

for any $c > 0$. Enforcement of the requirement for normalization of the vector leads to the unique solution $_{opt} \mathbf{G}^{*(k)}$.

Having determined $_{opt}^n \mathbf{G}^{(k)}$, it remains to determine the optimal value of the parameters $G_0^{(k)}$ for every k , to complete the model of Def. S4.1. We use the fact that

$$Q(C_t^{(k)}) = \int_{\phi^{(k)}} q(\phi^{(k)}, C_t^{(k)}) d\phi^{(k)} \quad (\text{S62})$$

To solve for the parameter $G_0^{(k)}$, we introduce it by using, as per the model, the estimate

$$q(\phi^{(k)}, C_t^{(k)}) \approx \hat{q}(\phi^{(k)}, C_t^{(k)}; {}^{n+1}\mathbf{G}^{(k)}) = \frac{(u_t^{(k)} + G_0^{(k)})^+}{2}. \quad (\text{S63})$$

$u_t^{(k)} = \cos \phi^{(k)} \leq 0$ for $\frac{\pi}{2} \leq \phi^{(k)} \leq \frac{3\pi}{2}$. If $G_0^{(k)} \leq 0$, which is true, as we show at the end of this Theorem's proof, then the curve of $y = u_t^{(k)} + G_0^{(k)}$ is the curve of $y = \cos \phi^{(k)}$, shifted lower by $|G_0^{(k)}|$. This

implies firstly that $u_t^{(k)} + G_0^{(k)} = 0$ when $\phi^{(k)} = \arccos(-G_0^{(k)})$, and secondly that $0 \leq \arccos(-G_0^{(k)}) \leq \frac{\pi}{2}$. This curve, i.e. $u_t^{(k)} + G_0^{(k)}$, is now non-negative only for $0 \leq \phi^{(k)} \leq \arccos(-G_0^{(k)})$ and for $\frac{3\pi}{2} + \arccos(-G_0^{(k)}) \leq \phi^{(k)} \leq 2\pi$. So,

$$Q(C_t^{(k)}) = \int_0^{\arccos(-G_0^{(k)})} \frac{\cos \phi^{(k)} + G_0^{(k)}}{2} d\phi^{(k)} \\ + \int_{\frac{3\pi}{2} + \arccos(-G_0^{(k)})}^{2\pi} \frac{\cos \phi^{(k)} + G_0^{(k)}}{2} d\phi^{(k)} \\ = 2 \cdot \frac{1}{2} \left(\sin \phi^{(k)} + G_0^{(k)} \phi^{(k)} \right) \Big|_0^{\arccos(-G_0^{(k)})} \\ = \sin \arccos(-G_0^{(k)}) + G_0^{(k)} \arccos(-G_0^{(k)}) \quad (\text{S64})$$

$$\iff Q(C_t^{(k)}) \\ = \sqrt{1 - (G_0^{(k)})^2} + G_0^{(k)} \arccos(-G_0^{(k)}). \quad (\text{S65})$$

by demanding that $Q(C_t^{(k)}) = P(C_t^{(k)}) \quad \forall k$, this proves Eq. S39 of the Theorem. This equation cannot be solved for $G_0^{(k)}$ analytically.

Our experimental results (see main paper, "Application to video recognition" section) show that the model can function well in practice without updating the bias or threshold parameters $G_0^{(k)}$. Still, here, we do derive an approximation of $G_0^{(k)}$ as a function of $P(C_t^{(k)})$. We find from Eq. S39 that $G_0^{(k)} = -1 \implies P(C_t^{(k)}) = 0$ and $G_0^{(k)} = 0 \implies Q(C_t^{(k)}) = 1$. In addition, numerically, we find that $P(C_t^{(k)})$ is an increasing function of $G_0^{(k)}$.

We will now quantify how non-linear this curve of Eq. S39 is, in order to assess how reasonable it is to use a line as an estimate of the curve. The line that passes through the two points that we specified on the $(G_0^{(k)}, P(C_t^{(k)}))$ plane, namely the points $(-1, 0)$ and $(0, 1)$, is described by $\widehat{P(C_t^{(k)})} = \widehat{G_0^{(k)}} + 1$, i.e. it has a derivative equal to 1. We find that the derivative of the curve of Eq. S65 is $\frac{\partial Q(C_t^{(k)})}{\partial G_0^{(k)}} = \arccos(-P(C_t^{(k)}))$. In the range $-1 \leq G_0^{(k)} \leq 0$, the derivative increases from a value of 0 at $G_0^{(k)} = -1$, and crosses the value of 1 at $G_0^{(k)} = -\cos(1)$. I.e., the curve initially diverges from the straight line, and at the point $G_0^{(k)} = -\cos(1)$ it begins to converge. Therefore, at this point the line has its maximum distance from the curve. Specifically, the difference between the value of $P(C_t^{(k)})$ at this point and its approximation $\widehat{P(C_t^{(k)})}$ by the line is equal to $\cos(1) - \sqrt{\sin^2(1) - \cos(1)}$ which, compared to the real value $P(C_t^{(k)}) = \sqrt{\sin^2(1) - \cos(1)}$ is a 31.9% overestimation by the line, and that is the maximum divergence of the line, showing that it can be reasonable to use the line

$$_{opt} \widehat{G_0^{(k)}} = P(C_t^{(k)}) - 1 \quad \forall k \quad (\text{S66})$$

as an approximation of the optimal value $_{opt} G_0^{(k)}$ of parameter $G_0^{(k)}$. ■

Our derivation relied on the assumption that $G_0^{(k)} \leq 0$. We will show now that this is true.

$$\hat{q}(\phi^{(k)}, C_t^{(k)}; {}^{n+1}\mathbf{G}^{(k)}) \approx q(\phi^{(k)}, C_t^{(k)}) \quad (\text{S67})$$

$$\implies (\cos \phi^{(k)} + G_0^{(k)})^+ \\ \approx (\cos \phi^{(k)})^+ Q(C_t^{(k)}) \leq (\cos \phi^{(k)})^+ \quad (\text{S68})$$

$$\implies G_0^{(k)} \leq 0. \quad (\text{S69})$$

S4.2 The optimal parameters given the history of observations

Theorem S4.2. Let it be $\mathbf{W} := E_{p_B^{(k)}}[\mathbf{X}_t]$, and $W_0^{(k)} := P(C_t^{(k)}|B) - 1$. The optimal parameters of the model of Definition S4.1, for data following the assumptions of paragraph S1.1, are, for each component k ,

$$\begin{aligned} & \text{}_{opt}^n \mathbf{G}^{(k)} \\ &= \frac{1}{\beta (W_0^{(k)} + 1)} \sum_{i=1}^T \mathbf{X}_{t_i} Q_{t_i}(C^{(k)}) f(t - t_i) + \mathbf{W}^{(k)}, \quad (\text{S70}) \end{aligned}$$

and

$$\begin{aligned} & \text{}_{opt} G_0^{(k)} \approx \widehat{\text{}_{opt} G_0^{(k)}} \\ &= \frac{\beta}{\sum_{i=1}^T f(t - t_i) + \beta} \\ &\cdot \left(\sum_{i=1}^T (Q_{t_i}(C^{(k)}) - 1) \frac{f(t - t_i)}{\beta} + W_0^{(k)} \right), \quad (\text{S71}) \end{aligned}$$

$$\text{where } Q_t(C^{(k)}) = \frac{\max(u_t^{(k)} + G_0^{(k)}, 0)}{\sum_{l=1}^K \max(u_t^{(l)} + G_0^{(l)}, 0)}. \quad (\text{S72})$$

Proof. Theorem S4.1 indicates that

$$\text{}_{opt} \mathbf{G}^{(k)} = c \cdot E_{p^{(k)}}[\mathbf{X}_t], \quad c > 0 \quad (\text{S73})$$

for every k , where $\mathbf{X}_t \sim p(\mathbf{X}_t)$ from Eq. S7. As in the proof of Theorem S3.2, we can use Eq. S30, the fact that $E_{\mathcal{N}(\mathbf{x}_{t_i}, \Sigma_{t_i, t})}[\mathbf{X}_t] = \mathbf{X}_{t_i}$, and, as an estimate of $P(C_{t_i}^{(k)}|\mathbf{X}_{t_i}, \mathcal{X}_{t_i}, \mathcal{C}_{t_i})$, the model of Definition S4.1, to find the parameters $\text{}_{opt} \mathbf{G}^{(k)}$ for this data distribution $p(\mathbf{X}_t)$, given past observations.

For each time instance t_i , $P(C_{t_i}^{(k)}|\mathbf{X}_{t_i}, \mathcal{X}_{t_i}, \mathcal{C}_{t_i})$ can be estimated by using

$$Q_t(C^{(k)}) := Q(C_t^{(k)}|\mathbf{X}_t, {}^{n+1}\mathbf{G}_t), \quad (\text{S74})$$

if the optimal parameters are known. For this, we will now derive the parametric form of $Q_t(C^{(k)})$. From Bayes' rule, it is

$$\begin{aligned} Q_t(C^{(k)}) &= \frac{q(\mathbf{X}_t, C_t^{(k)}, {}^{n+1}\mathbf{G}_t^{(k)})}{q(\mathbf{X}_t; {}^{n+1}\mathbf{G}_t)} \\ &= \frac{q(\mathbf{X}_t, C_t^{(k)}, {}^{n+1}\mathbf{G}_t^{(k)})}{\sum_{l=1}^K q(\mathbf{X}_t, C_t^{(l)}, {}^{n+1}\mathbf{G}_t^{(l)})}, \quad (\text{S75}) \end{aligned}$$

where $q(\mathbf{X}_t, C_t^{(k)}, {}^{n+1}\mathbf{G}_t^{(k)})$ is approximated by the model of Definition S4.1 as

$$q(\mathbf{X}_t, C_t^{(k)}, {}^{n+1}\mathbf{G}_t^{(k)}) \approx \frac{1}{2} \max(u_t^{(k)} + G_0^{(k)}, 0) \quad (\text{S76})$$

i.e.

$$Q_t(C^{(k)}) = \frac{\max(u_t^{(k)} + G_0^{(k)}, 0)}{\sum_{l=1}^K \max(u_t^{(l)} + G_0^{(l)}, 0)}. \quad (\text{S77})$$

Let

$$W_0^{(k)} := P(C_t^{(k)}|B) - 1, \quad (\text{S78})$$

and let

$$\mathbf{W}^{(k)} := E_{p_B^{(k)}}[\mathbf{X}_t]. \quad (\text{S79})$$

Then, using the definition of Eq. S30, we find

$$E_{p_t^{(k)}}[\mathbf{X}_t] = \frac{1}{Z_t^{(k)}} \left(\sum_{i=1}^T \mathbf{X}_{t_i} P(C_{t_i}^{(k)}|\mathbf{X}_{t_i}, \mathcal{X}_{t_i}, \mathcal{C}_{t_i}) f(t - t_i) \right.$$

$$\left. + \beta \mathbf{W}^{(k)} (W_0^{(k)} + 1) \right). \quad (\text{S80})$$

Therefore, because

$$\text{}_{opt}^n \mathbf{G}^{(k)} = c \cdot E_{p^{(k)}}[\mathbf{X}_t] \quad (\text{S81})$$

for any chosen positive c , we can choose c such that

$$\begin{aligned} & \text{}_{opt}^n \mathbf{G}^{(k)} \\ &= \frac{1}{\beta (W_0^{(k)} + 1)} \sum_{i=1}^T \mathbf{X}_{t_i} Q_{t_i}(C^{(k)}) f(t - t_i) + \mathbf{W}^{(k)}, \quad (\text{S82}) \end{aligned}$$

where we used the model $Q_{t_i}(C^{(k)})$ as an estimate of $P(C_{t_i}^{(k)}|\mathbf{X}_{t_i}, \mathcal{X}_{t_i}, \mathcal{C}_{t_i})$. This proves Eq. S70 of the Theorem.

We will now also find the optimal bias parameters $\text{}_{opt} G_0^{(k)}$. In Theorem S4.1 we showed that this can be approximated relatively well as

$$\text{}_{opt} G_0^{(k)} \approx \widehat{\text{}_{opt} G_0^{(k)}} = P(C_t^{(k)}) - 1. \quad (\text{S83})$$

Therefore, using

$$P(C_t^{(k)}) = \sum_{i=1}^T P(C_t^{(k)}|A_{t_i}) P(A_{t_i}) + P(C_t^{(k)}|B) P(B) \iff \quad (\text{S84})$$

$$P(C_t^{(k)}) = \frac{\sum_{i=1}^T P(C_{t_i}^{(k)}|\mathbf{X}_{t_i}, \mathcal{X}_{t_i}, \mathcal{C}_{t_i}) f(t - t_i) + \beta (W_0^{(k)} + 1)}{\sum_{i=1}^T f(t - t_i) + \beta}, \quad (\text{S85})$$

we find that

$$\begin{aligned} \text{}_{opt} G_0^{(k)} &\approx \frac{\sum_{i=1}^T P(C_{t_i}^{(k)}|\mathbf{X}_{t_i}, \mathcal{X}_{t_i}, \mathcal{C}_{t_i}) f(t - t_i) + \beta (W_0^{(k)} + 1)}{\sum_{i=1}^T f(t - t_i) + \beta} - 1 \\ &= \frac{\beta}{\sum_{i=1}^T f(t - t_i) + \beta} \\ &\cdot \left[\sum_{i=1}^T (P(C_{t_i}^{(k)}|\mathbf{X}_{t_i}, \mathcal{X}_{t_i}, \mathcal{C}_{t_i}) - 1) \frac{f(t - t_i)}{\beta} + W_0^{(k)} \right]. \quad (\text{S86}) \end{aligned}$$

By making use of the model $Q_t(C^{(k)})$ as an estimate of $P_t(C^{(k)})$ in Eq. S86, we prove Eq. S71 of the Theorem. ■

S5 Clustering interpretation of the model and of its optimization: Elastic Clustering

for all centroids k do

${}^{n+1}\mathbf{F}_k \leftarrow \mathbf{0}$

${}^{n+1}\mathbf{G}_k \leftarrow {}^{n+1}\mathbf{W}_k$ {Initialize centroids. eg with EM}

for $t = 1$ to duration do

${}^{n+1}\mathbf{F}_k \leftarrow {}^{n+1}\mathbf{F}_k - \lambda \cdot {}^{n+1}\mathbf{F}_k$ {Elastically relax F}

$\mathbf{G}_k \leftarrow \mathbf{W}_k + \mathbf{F}_k$ {Update generative model}

$G_{0k} \leftarrow (W_{0k} + F_{0k})/Z_{0kt}$ { Z_{0kt} for possible normalization}

input \mathbf{X}

if \mathbf{X} is not $\mathbf{0}$ then

for all centroids k do

$u_k \leftarrow u(\mathbf{X}, \mathbf{G}_k)$ {Proximity}

$q_{Xk} \leftarrow q(u_k, G_{0k})$ {Joint probability}

$q_all \leftarrow$ set of all q_{Xk}

for all centroids k do

$Q_k \leftarrow Q(q_{Xk}, q_all)$ {Inference. eg Q=softmax or max}

$\mathbf{F}_k \leftarrow \mathbf{F}_k + \gamma \mathbf{X} Q_k$ {Input-centroid attraction}

$F_{0k} \leftarrow F_{0k} + \gamma Q_k$

Algorithm 1: Elastic Clustering

Both the exponential and the linear model, i.e. Eq. S24 and Eq.

S70 show that $_{opt} \mathbf{G}^{(k)}$ is the weighted average of two points in the n -dimensional space, one being the fixed term $\mathbf{W}^{(k)}$ and the other being a dynamic term, specifically a discrete convolution of $\mathbf{X}_{t_i} Q_{t_i}(C^{(k)})$ with $f(t)$, be it $\mathbf{F}_t^{(k)}$:

$$\mathbf{G}_t^{(k)} = \mathbf{F}_t^{(k)} + \mathbf{W}^{(k)}. \quad (\text{S87})$$

From the same Eq. S24 or Eq. S70 it can be seen that, at every posterior inference result $Q_t^{(k)}$, the dynamic term is incremented as follows:

$$\mathbf{F}_t^{(k)} \leftarrow \mathbf{F}_t^{(k)} + \gamma \mathbf{X}_t Q_t^{(k)}, \quad (\text{S88})$$

where γ is a positive constant, specifically $\gamma := \frac{f(0)}{\beta e^{w_0^{(k)}}}$ in the case of the exponential model (Eq. S24), and $\gamma := \frac{f(0)}{\beta (w_0^{(k)} + 1)}$ in the case of the linear model (Eq. S70). In addition, this term $\mathbf{F}_t^{(k)}$ subsequently decays continuously according to the dynamics of $f(t)$, such that $\mathbf{G}_t^{(k)}$ relaxes towards the fixed resting point $\mathbf{W}^{(k)}$. If $f(t)$ is exponential with a rate λ , then

$$\frac{d\mathbf{F}_t^{(k)}}{dt} = -\lambda \mathbf{F}_t^{(k)}. \quad (\text{S89})$$

Eq. S88 shows that each input \mathbf{X}_{t_i} attracts $\mathbf{G}^{(k)}$ in proportion to the inferred probability $Q_{t_i}(C^{(k)})$ that \mathbf{X}_{t_i} 's label was $C^{(k)}$. In addition, the attraction by each past input is in proportion to the value of a temporally evolving kernel $f(t)$. f ultimately decays to zero, as assumed in Section S1.1, Assumption 7, for example exponentially. That is, the movement of $\mathbf{G}^{(k)}$ towards the inputs is elastic, as the dynamics is relaxation of $\mathbf{G}^{(k)}$ towards a resting point $\mathbf{W}^{(k)}$. Therefore, the model can be described as a sequential clustering algorithm based on elastic centroids (Fig. 2a and Algorithm 1). Every input is associated by the algorithm with each cluster to a degree $Q_t^{(k)}$ that depends on the proximity of the input vector to the centroid. If the proximity function for the clustering is specifically chosen to be the cosine similarity, then the Elastic Clustering can compute the optimal parameters of the two generative models we described in S3.1 and S4.1. In particular, if $Q_t^{(k)}$ is implemented as in Eq. S26, and in turn its bias parameter $G_{0t}^{(k)}$ also adapts to the input elastically with time as per Eq. S25, then the clustering algorithm realizes the exponential model and the associated Bayesian optimization that were described in Section S3. On the other hand, if $Q_t^{(k)}$ is instead implemented as in Eq. S72, and its bias parameter adapts as per Eq. S71, then the clustering algorithm realizes and approximately optimizes the linear model of Section S4.

S6 Neurosynaptic equivalence of the optimal model: ST-STDP

S6.1 Stochastic or spiking input

The model remains functional if we assume that the samples \mathbf{X}_t are not visible to the observer, but what is visible instead is a stochastic measurement \mathbf{X}_t^{stoch} , drawn randomly from a probability distribution whose mean is the underlying data point: $E[\mathbf{X}_t^{stoch}] = \mathbf{X}_t$. An example of such inputs are Poisson-distributed rate-coded spiking inputs, a common method of input coding in models of SNNs,^{32,34} as well as a good model of biological rate-coding neurons.^{48–50} To use the Elastic Clustering model, we need an estimate of the – now hidden – measured data point \mathbf{X}_t . If the measurement distribution were stationary, then the underlying data point could be estimated as the uniformly weighted average of the noisy measurements over the past. However, as each object is transformed, and the object that is visible switches, the measurement distribution cannot be assumed stationary. Instead, the

estimate of the data point is

$$\begin{aligned} \mathbf{X}_t &= E[\mathbf{X}_t^{stoch}] = \int \mathbf{X}^{stoch} p(\mathbf{X}^{stoch}) d\mathbf{X}^{stoch} \\ &= \int_{\tau=0}^t \mathbf{X}_{t-\tau}^{stoch} p(\mathbf{X}_t = \mathbf{X}_{t-\tau}) d\tau. \end{aligned} \quad (\text{S90})$$

$p(\mathbf{X}_t = \mathbf{X}_{t-\tau})$ can be derived from the dynamics of the objects in the environment.

$$\begin{aligned} p(\mathbf{X}_t = \mathbf{X}_{t-\tau}) &= p(\mathbf{X}_t = \mathbf{X}_{t-\tau} | O_t = O_{t-\tau}) P(O_t = O_{t-\tau}) \\ &\quad + p(\mathbf{X}_t = \mathbf{X}_{t-\tau} | O_t \neq O_{t-\tau}) P(O_t \neq O_{t-\tau}) \\ &= p(\mathbf{X}_t = \mathbf{X}_{t-\tau} | O_t = O_{t-\tau}) e^{-\alpha\tau}, \end{aligned} \quad (\text{S91})$$

because the observed objects are replaced according to a Poisson process of rate α (Section S1.1, Assumption 6), and because $p(\mathbf{X}_t = \mathbf{X}_{t-\tau} | O_t \neq O_{t-\tau}) = 0$. But we have concluded in the proof of Theorem S2.1 that, due to the assumptions of continuity, each object is generated by an underlying Wiener process. So the resulting probability density function is a multivariate Gaussian:

$$\begin{aligned} p(\mathbf{X}_t | \mathbf{X}_{t_i}, O_t = O_{t_i}) &\equiv \mathcal{N}(\mathbf{X}_{t_i}, \Sigma_{t_i,t}) \\ &= \frac{\exp(-\frac{1}{2}(\mathbf{X}_t - \mathbf{X}_{t_i})^T \Sigma_{t_i,t}^{-1} (\mathbf{X}_t - \mathbf{X}_{t_i}))}{\sqrt{(2\pi)^n |\Sigma_{t_i,t}|}}, \end{aligned} \quad (\text{S92})$$

where $\Sigma_{t_i,t}$ is the covariance matrix of the distribution, whose determinant $|\Sigma_{t_i,t}|$ increases linearly with time $\tau = t - t_i$ with some positive rate σ^2 , i.e. $|\Sigma_{t_i,t}| = \sigma^2 \tau$. Thus, because \mathbf{X}_{t_i} is the mean of this distribution, it follows that

$$p(\mathbf{X}_t = \mathbf{X}_{t_i} | \mathbf{X}_{t_i}, O_t = O_{t_i}) = \frac{1}{\sqrt{(2\pi)^n \sigma^2 \tau}}. \quad (\text{S93})$$

So, using this result in Eq. S91, we conclude from Eq. S90, that the underlying data point at time t is estimated as proportional to the weighted integral of past measurements, where the weightings decay with $\tau^{-1/2}$ and with $e^{-\alpha\tau}$:

$$\mathbf{X}_t = \frac{1}{(2\pi)^{n/2} \cdot \sigma} \int_{\tau=0}^t \mathbf{X}_{t-\tau}^{stoch} \tau^{-1/2} e^{-\alpha\tau} d\tau. \quad (\text{S94})$$

This estimate of the input, used with Eq. S24, enables the estimation of the optimal parameters, when inputs are stochastic measurements.

S6.2 Equivalence to Short-Term Hebbian plasticity

The cosine similarity between the input vector and each centroid's parameters underpins both the exponential and the linear model. This similarity is precisely computed by a linear neuron that receives normalized inputs $\mathbf{X}_t^* := \frac{\mathbf{X}_t}{\|\mathbf{X}_t\|}$, and that normalizes its vector of synaptic efficacies: $\mathbf{G}_t^{*(k)} := \frac{\mathbf{G}_t}{\|\mathbf{G}_t\|}$. The cosine similarity is then the neuron's summed weighted input: $u_t^{(k)} = \mathbf{G}_t^{*(k)} \cdot \mathbf{X}_t^*$. Then, a set of K such neurons in a soft-max configuration, each with a bias term $G_{0t}^{(k)}$, computes the functions $Q_t^{(k)}$ of the exponential model (Section S3, Eq. S26). The soft-max-configured neurons implement and optimize the Bayesian generative model and the equivalent clustering model, if their parameters are set according to Eq. S24. The function $Q_t^{(k)}$ of the linear model (Section S4, Eq. S72) can also be computed neurally. In particular, a rectified linear unit (ReLU) with normalized inputs and synaptic efficacies can compute the function $(u_t^{(k)} + G_{0t}^{(k)})^+ = \max(u_t^{(k)} + G_{0t}^{(k)}, 0)$ and thus a set of k such ReLU units can compute the ratio-based function of Eq. S72.

Furthering the neural analogy, Eq. S24 and Eq. S70 show that, in both models, neuron k has a resting weight vector $\mathbf{W}^{(k)}$. It also shows that for a pair of input \mathbf{X}_{t_i} and subsequent neuronal

output $Q_i(C^{(k)})$, each element of the parameter vector, i.e. the overall efficacy $G^{(jk)} = W^{(jk)} + F^{(jk)}$ of the j -th synapse, changes by a quantity proportional to both the pre-synaptic input and the immediately subsequent post-synaptic neuron's output (also summarized in Eq. S88). This is a Hebbian update similar to an STDP rule with a very short window for the timing dependence. The dynamics of the bias term for both models (Eq. S25, and, respectively, Eq. S71) are a form of Hebbian short-term sensitization of the neuron with each input, that also depends on the output $Q_i(C^{(k)})$.

If inputs are stochastic, e.g. rate-coded spike trains, using Eq. S94 with Eq. S24 or Eq. S70, shows that a synaptic efficacy increment occurs for each pair of pre- and post-synaptic activity (Fig. 1d-f), with a timing dependence (Fig. 2b) such that the increment becomes smaller for longer time intervals τ elapsed between pre- and post-, specifically decaying with $v(\tau) = \tau^{-1/2}e^{-\alpha\tau}$. Such a time-dependent change of the synaptic efficacy is STDP, in a generalized form that can involve non-spiking, i.e. analog pre-synaptic input $X_{t_i-\tau}^{(j)}$ of synapse j and analog post-synaptic activation $Q^{(k)}$ of neuron k . Compared to standard STDP that is based on spikes, the effect of the non-binary pre- and post-synaptic activity pair is the rescaling of the synaptic update not only by the temporal distance within the pair, but also by the analog values $X_{t_i-\tau}^{(j)}$ (or $X_{t_i-\tau}^{stoch(j)}$) and $Q^{(k)}(t_i)$, as is described in Eq. S24 and Eq. S70 for the exponential and the linear model respectively. In addition, the same Eq. shows that the synaptic update is transient (Fig. 2c, and Fig. 1g-h) and decays exponentially with a time constant of $\frac{1}{\beta}$. This, therefore, is a case of STP, and combined with the STDP effect, it is a case of ST-STDP, in a generalized form that can involve non-spiking inputs and non-spiking neuronal activations.

S6.3 Implementation with spiking neurons

In this section we describe how, in addition to spiking *input* (Section S6.1), spiking *output* can also be used, to derive a stochastic approximation of the optimal model. To achieve this, we arrange spiking neurons in a winner-take-all (WTA) setup (Fig. 3b) — a powerful SNN architecture.^{34,55} Such an SNN, when equipped with STDP, can approximate EM.³² Thus, regular, i.e. long-term, STDP can be used here as well to learn the initial resting weights $W^{(jk)}$. After the training, during the testing phase, short-term dynamics are added to the synapses, enabling ST-STDP. Making arguments similar to those in,³² we will show that in this set-up too, the network does compute the necessary probabilities, here in order to implement the Elastic Clustering, in the specific form that maintains an optimized Bayesian generative model. We use a stochastic model, in which the input firing rate is proportional to \mathbf{X}_t 's analog value, and the output neurons' firing probability is a function of the membrane potential $u^{(k)}$. Each input spike arriving at synapse j causes an excitatory post-synaptic potential modelled as a step function of amplitude equal to the synaptic efficacy $G^{(jk)}$ with a short duration. WTA competition between the neurons ensures that no more than one of the output neurons can fire at a time. This competition is mediated by a lateral inhibition term $I(t)$ that is common to all neurons.

Stochastic exponential spiking neurons To implement the spiking analogue to the exponential model, for normalized input \mathbf{X}_t^* , the membrane potential of a neuron k is $u_t^{(k)} = \mathbf{G}^{*(k)} \cdot \mathbf{X}_t^* + G_0^{(k)} - I(t)$, where $G_0^{(k)}$ is the neuron's intrinsic excitability. The output neurons are exponential, i.e. each neuron's spiking behaviour is modelled as an inhomogeneous Poisson process with

a firing rate

$$r^{(k)} = e^{u^{(k)}} = \frac{e^{\mathbf{G}^{*(k)} \cdot \mathbf{X}_t^* + G_0^{(k)}}}{e^I} = Q(C_t^{(k)}; G_0^{(k)}) \frac{q^{(k)}}{e^I}, \quad (\text{S95})$$

which uses the model's Definition S3.1. The combined firing output of the K neurons is a Poisson process with rate $r_{all} = \sum_{l=1}^K r^{(l)}$. Therefore, if at one time instance the network produces an output spike, the conditional probability that this spike originated from neuron k is

$$\frac{r^{(k)}}{r_{all}} = \frac{e^{\mathbf{G}^{*(k)} \cdot \mathbf{X}_t^* + G_0^{(k)}}}{\sum_{l=1}^K e^{\mathbf{G}^{*(l)} \cdot \mathbf{X}_t^* + G_0^{(l)}}}, \quad (\text{S96})$$

which is independent of the inhibition term. Importantly, this is in fact exactly $Q_t(C^{(k)})$ as given in Eq. S26. Thus, each output spike is a sample from the $Q^{(k)}$ distribution, so that the emission or not of a spike by neuron k at time t can be used in Eq. S24 as an instantaneous stochastic estimate of $P_t(C^{(k)})$.

Leaky integrate-and-fire neurons The rectified linear model can also be extended to spiking outputs, as the exponential model was extended in Paragraph S6.3. Here too, we use a stochastic model in which the input firing rate is proportional to the input's analog value, but here the output neurons' firing probability is a ReLU function of the membrane potential $u^{(k)}$. Here too the stochastic spiking ReLU neurons are configured in a WTA connectivity, such that competition between the neurons ensures that at each time instance no more than one of the output neurons can fire, and this competition too is mediated by an inhibition term that is common to all neurons. However, in this case inhibition is divisive, so that the membrane potential of a neuron k is

$$u^{(k)}(t) = \frac{\mathbf{G}^{*(k)} \cdot \mathbf{X}_t^* + G_0^{(k)}}{I(t)}. \quad (\text{S97})$$

This is in accordance with a multitude of studies that have described and modelled evidence for divisive effects of inhibition on neuronal gains.⁵⁹⁻⁶¹ We model each output neuron's spiking behaviour as an inhomogeneous Poisson process with a firing rate

$$R^{(k)} = \text{ReLU}(u^{(k)}) = \frac{\text{ReLU}(\mathbf{G}^{*(k)} \cdot \mathbf{X}_t^* + G_0^{(k)})}{I(t)}. \quad (\text{S98})$$

The combined firing output of the K neurons is a Poisson process with rate $R_{all} = \sum_{l=1}^K R^{(l)}$. Therefore, if at some time instance t the network produces an output spike, the conditional probability that this spike originated from neuron k can be expressed as

$$\frac{R^{(k)}}{R_{all}} = \frac{\text{ReLU}(\mathbf{G}^{*(k)} \cdot \mathbf{X}_t^* + G_0^{(k)})}{\sum_{l=1}^K \text{ReLU}(\mathbf{G}^{*(l)} \cdot \mathbf{X}_t^* + G_0^{(l)})}, \quad (\text{S99})$$

which is independent of the inhibition term. This is in fact exactly $Q_t(C^{(k)})$ as given in Eq. S77. Thus, each output spike is a sample from the $Q^{(k)}$ distribution, so that the emission or not of a spike by neuron k at time t can be used in Eq. S70 as the value of $Q_t(C^{(k)})$ i.e. as an instantaneous stochastic inference of $P_t(C^{(k)})$ in Eq. S82.

Notably, a LIF spiking neuron's firing rate is linearly dependent on the weighted input for inputs that well surpass the firing threshold,⁶² and it is zero below threshold. Assuming stochastic inputs, a LIF neuron's output is stochastic, with a probability of producing a spike within an infinitesimal time window proportional to its firing rate. Therefore, the stochastic spiking ReLU neuronal model is a close approximation of a LIF neuron with noisy inputs, which, in turn, is a convenient model commonly used for simulations or emulations of spiking neurons. This makes our model efficiently testable in practice using standard LIF neurons in simulations.

Short-term STDP The spiking outputs combined with the spiking inputs render the plasticity in the spiking realization of the model indeed an STDP rule, with an additional short-term temporal dependence. The updates are event-based, such that at every post-synaptic spike, the synapses are updated according to the spikes they received previously, the STDP kernel $v(\tau) = \tau^{-1/2}e^{-\alpha\tau}$, and the time τ that mediated between the pre- and post-synaptic spikes (Eq. S88 and Eq. S94). The un-normalized synaptic efficacy $G_j^{(k)}$ of synapse j subsequently decays towards the fixed weight $W_j^{(k)}$ according to the short-term plasticity dynamics $f(t)$.

S7 Weight-dependent ST-STDP

The uninformed prior belief about an object's transformation has characteristics of a Wiener process with no drift and implies a normal distribution $\mathcal{N}(\mathbf{X}_{t_i}, \Sigma_{t_i,t})$, centred around the most recent observation \mathbf{X}_{t_i} of the object. In a more general formulation of the model, Assumption 4 from Section S1.1 may include some prior knowledge about the temporal evolution of an object. An informed prior would instead lead to a distribution centred around a mean point $\mathbf{X}'_{t_i} = g(\mathbf{X}_{t_i}|\boldsymbol{\theta})$, according to a function g of the input, parametrized by $\boldsymbol{\theta}$.

For example, it may be $\mathbf{X}'_{t_i} = g(\mathbf{X}_{t_i}) = \boldsymbol{\theta} \circ \mathbf{X}_{t_i}$, $\boldsymbol{\theta}, \mathbf{X}_{t_i} \in \mathbb{R}$, where \circ symbolizes the element-wise product, i.e. where each dimension $X_{t_i}^{(j)}$ of \mathbf{X}_{t_i} is weighted by a different coefficient $\theta^{(j)}$.

The weighted influence of each input feature on future samples, as represented by $\boldsymbol{\theta}$, is determined by a prior likelihood distribution of the input feature, and this prior may be according to the history-independent distribution $p(\mathbf{X}_t|B)$ of Eq. S6. This describes situations where a feature of an observation of the k -th class is more likely to be repeated if it is generally a likely feature of observations of that k -th class, than if it is not, and this likelihood is reflected in the distribution $p(\mathbf{X}_t|C^{(k)}, B)$. In this case, we can formulate this aspect of the data as

$$\mathbf{X}'_{t_i} = g(\mathbf{X}_{t_i}, \boldsymbol{\theta}^{(k)}) = \boldsymbol{\theta}^{(k)} \circ \mathbf{X}_{t_i}, \quad (\text{S100})$$

where

$$\theta^{(jk)} = c + (1 - c)W^{(jk)}, j = 1, 2, \dots, n \quad (\text{S101})$$

and $c < 1$.

$\mathbf{X}'_{t_i}^{(k)}$ is then the datapoint that is used in place of \mathbf{X}_{t_i} in the expressions of the parameter dynamics, and the one that attracts the k -th centroid, so that the Hebbian update of Eq. S88 becomes

$$\mathbf{F}_t^{(k)} \leftarrow \mathbf{F}_t^{(k)} + \gamma \mathbf{X}'_{t_i}^{(k)} Q_t^{(k)} = \mathbf{F}_t^{(k)} + \gamma \boldsymbol{\theta}^{(k)} \circ \mathbf{X}_{t_i} Q_t^{(k)} \implies (\text{S102})$$

$$\mathbf{F}_t^{(jk)} \leftarrow \mathbf{F}_t^{(jk)} + \gamma^{(jk)} \mathbf{X}_{t_i}^{(k)} Q_t^{(k)}, \quad (\text{S103})$$

where $\gamma^{(jk)} = \gamma \theta^{(jk)}$. That is, the effect of incorporating such a prior knowledge is simply to let each synapse j have a different strength of the ST-STDP effect, equating $\gamma \theta^{(jk)}$, which is dependent on the fixed weight $W^{(jk)}$, i.e. the effect is to render ST-STDP weight-dependent. In data with transformations where novel features are as likely to be repeated, as typical features of an object type k , which would be the case if the objects' morphing is not biased by any prior distribution, then in Eq. S101, $c = 1$, and thus $\theta^{(jk)} = c$ which is equivalent to the original uninformed prior with a mean equal to the last observation of the object, i.e. from Eq. S100, $c = 1 \implies \mathbf{X}'_{t_i}^{(k)} = \mathbf{X}_{t_i}$, and there is no weight-dependence.

Eq. S100 and Eq. S101 are the forms that we used in the model of elastic clustering through ST-STDP on the OMNIST video, and they imply a simple weight-dependence involved in the short-term efficacy updates: a synapse with a stronger fixed (i.e. long-term) weight $W^{(jk)}$ is more strongly potentiated by the Hebbian (short-term) updates of the ST-STDP rule.

S8 Simulation differences from theory

To test the model, we chose to simulate it by using LIF neurons, which are a convenient model suitable for simulations, or implementations with efficient electronic circuits. The theoretically optimal model requires normalized inputs, continuous normalization of the synaptic efficacies, an additional inherent neuronal plasticity continuously updating the neuronal threshold (Eq. S71), and divisive inhibition in the case of LIF neurons, as opposed to subtractive. Nevertheless, our simulations used a simplified model without these particular idealities and demonstrated that the model can be robust to their absence. Omitting the neuronal memory mechanism that the intrinsic neuronal plasticity would introduce, not only simplified the simulation, but also allowed us to perform a more direct contrast of ST-STDP with other models such as RNNs or LSTMs which do include an analogous decaying neuronal memory, and therefore allows us to attribute the demonstrated benefits of the simulated model specifically to the synaptic plasticity mechanism.

S9 ST-STDP temporarily reshapes the internal representation of neurons

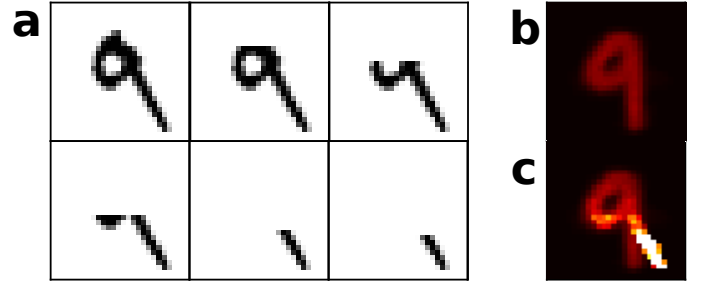


Figure S2: Example of temporary expansion of a neuron's internal representation. **a**, A sequence involving a handwritten digit "9" being progressively occluded. **b**, The weights of a neuron that has been trained to specialize in a handwritten form of digit 9. It can be seen that the learned pattern is different from the input digit (first frame of panel a). **c**, The efficacies of the same neuron during the last frame of a. Through ST-STDP, the neuron adapts its representation of digit 9 to match the different form of digit 9, and to recognize even the highly occluded last frame despite its very small overlap with the original learned weights. This expansion is short-term and, according to ST-STDP, the neuron's efficacy vector will relax to its original form after the specific input digit is replaced by a different one, or after the neuron stops recognizing it, i.e. stops firing in response to it.

Equipping neurons with ST-STDP allows them to temporarily change their internal representation, to learn the currently most accurate representation of the category they are already representing. This lets a neuron temporarily strengthen the most relevant of its permanent features it already has stored in its previously learned long-term weights, but it also allows the neuron to acquire new features that a current version of an object may have, but the neuron has not previously learned. An example of this is shown in (Fig. S2), where a neuron temporarily expands its internal representation (Fig. S2c) to be able to recognize a digit (digit 9) through a feature ('tail' of digit, last frame in Fig. S2a) that is not included in its long-term weights (Fig. S2b vs c). This possibility can be exploited to apply ST-STDP to other types of transformations than occlusions.

S10 ST-STDP realizes elastic clustering

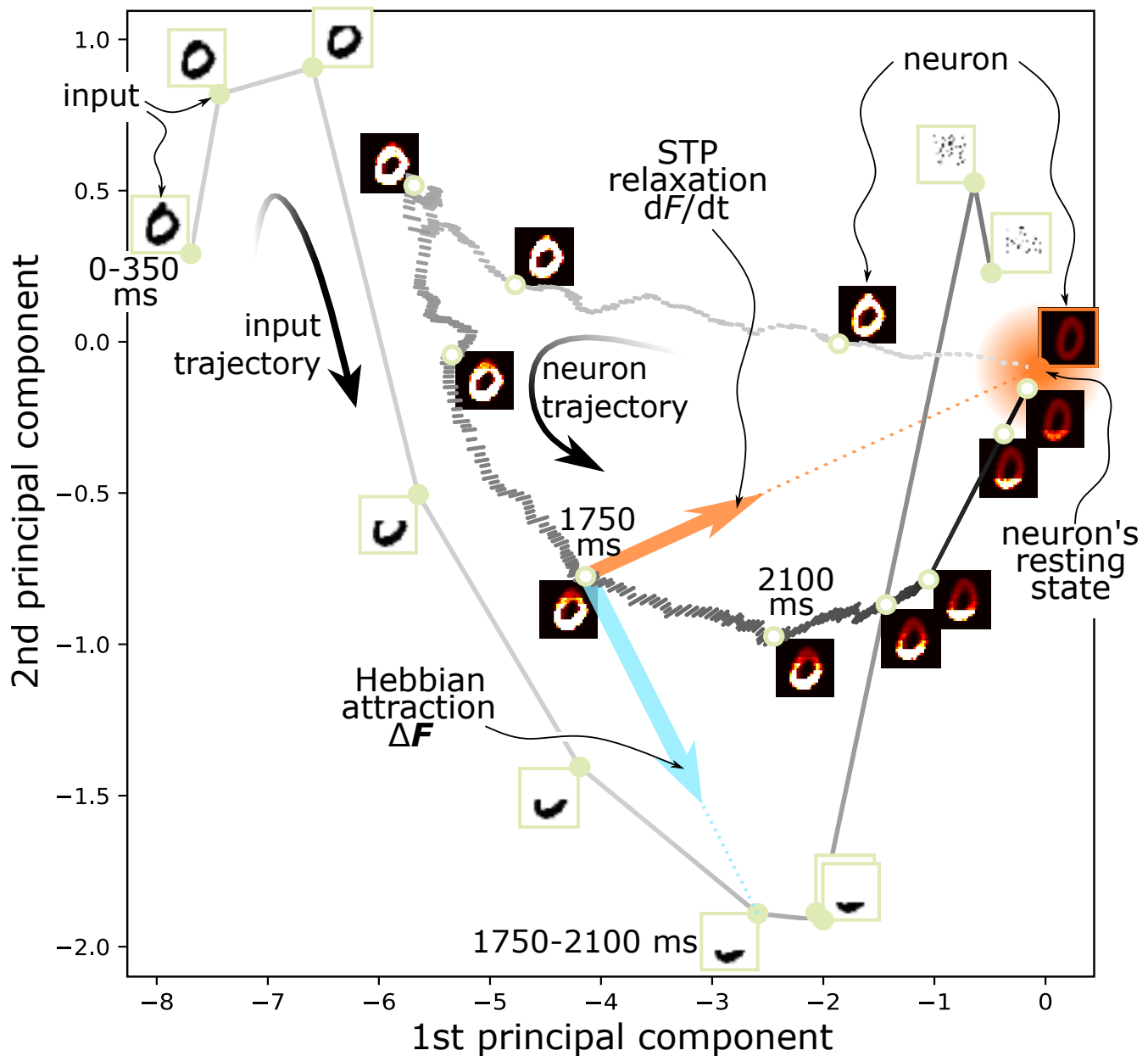


Figure S3: **Experimental confirmation that ST-STDP realizes elastic clustering.** (cf. Fig. 2a and Fig. 3.) The trajectory of a neuron's efficacy vector on the plane of the first two principal components, as it follows the input sequence and relaxes to its resting position, demonstrating qualitatively that the elastic clustering algorithm is indeed implemented by the simulated SNN. The input and neuron here are those of Fig. 3a and d. Green-filled circles beginning from the datapoint on the left-hand side (arrow labelled "input trajectory") correspond to the inputs of Fig. 3a. The neuron's initial and resting state is the orange highlighted point (right-hand side). The thick grey-scale sequence of points depicts the neuron's path (arrow labelled "neuron trajectory"). White-filled green circles correspond to Fig. 3d's snapshots. Grey points are the in-between states, plotted every 1 ms. Each time the neuron fires, it is attracted by the recent input (cyan arrow) through Hebbian plasticity, and thus follows the input's path. The STP (orange arrow) continuously tends to relax the neuron towards its resting state, which ultimately happens as the neuron stops firing (straight last segment of the neuron's trajectory).

S11 Application of elastic clustering to other types of transformations

OMNIST provides a demonstrative example of changing transformations that can be encountered in temporal data, and which can be tackled successfully by our elastic clustering and its implementation with spiking neurons. Our theoretical analysis shows that the strength of the approach is quite more general. As an example, it can be applied to the continuous recognition of patterns that morph with time, or whose observation changes because the sensor changes its properties with time. Here (Fig. S4) we show a proof-of-concept toy example where a neuron has been trained to recognize the side view of a person's face, but has never encountered its frontal view. As the head rotates though, the neuron, equipped with ST-STDP, expands its internal representation to match the rotating head, and to ultimately still recognize the frontal view, despite its lack of prior training on this pattern. This is a simple form of transfer learning, where the neuron used its previous knowledge of one view of the person, to learn a different one, by exploiting the common features between temporally contiguous input samples.

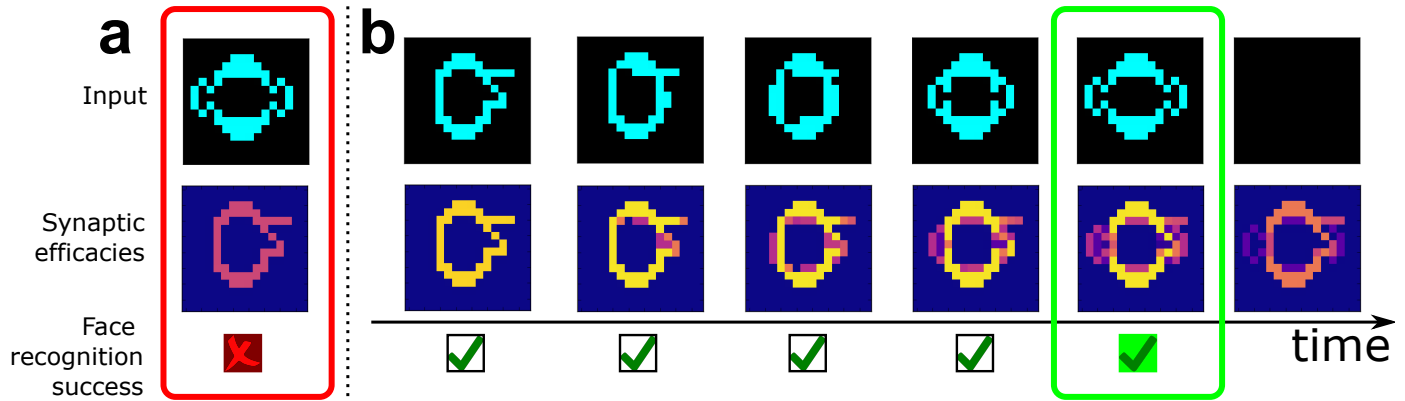


Figure S4: **Concept demonstration results of ST-STDP applied to morphing patterns.** **a**, One neuron has been pre-trained to recognize the side view of a person's face (middle), but the front view (top) can't be recognized (bottom) when it is presented out of context. **b**, Use of the temporal context through STP enables recognition. The side view is successfully recognized, and as the person rotates his head in subsequent frames, the face continues being recognized, even at its front view (green rectangle) that could not be recognized in panel A. This is possible thanks to the ST-STDP type of STP at the synapses. ST-STDP facilitates synapses whose inputs contribute to a successful face recognition (middle row). The facilitation is short-term, and the synapses that don't contribute to the postsynaptic neuron's activation transiently recover to their relaxed state (last frame).